Title

In vivo perturb-seq of cancer and microenvironment cells dissects oncologic drivers and radiotherapy responses in glioblastoma.

In vivo perturb-seq of cancer and microenvironment cells dissects oncologic drivers and radiotherapy responses in glioblastoma

S. John Liu[1,2,3], Christopher Zou[1,2], Joanna Pak[1,2], Alexandra Morse[4], Dillon Pang[4], Timothy Casey-Clyde[1,2,5], Ashir A. Borah[3,6], David Wu[2], Kyounghee Seo[1,2,5], Thomas O'Loughlin[9], Daniel A. Lim[2], Tomoko Ozawa[2], Mitchel S. Berger[2], Roarke A. Kamber[4], William A. Weiss[2,7], David R. Raleigh[1,2,5*†] and Luke A. Gilbert[3,8*†]

†David R. Raleigh and Luke A. Gilbert contributed equally to this work.

*Correspondence:
david.raleigh@ucsf.edu;
luke@arcinstitute.org

[1] Department of Radiation Oncology, University of California San Francisco, San Francisco, CA 94143, USA
[3] Arc Institute, Palo Alto, CA 94304, USA
Full list of author information is available at the end of the article

Abstract

Background: Genetic perturbation screens with single-cell readouts have enabled rich phenotyping of gene function and regulatory networks. These approaches have been challenging in vivo, especially in adult disease models such as cancer, which include mixtures of malignant and microenvironment cells. Glioblastoma (GBM) is a fatal cancer, and methods of systematically interrogating gene function and therapeutic targets in vivo, especially in combination with standard of care treatment such as radiotherapy, are lacking.

Results: Here, we iteratively develop a multiplex in vivo perturb-seq CRISPRi platform for single-cell genetic screens in cancer and tumor microenvironment cells that leverages intracranial convection enhanced delivery of sgRNA libraries into mouse models of GBM. Our platform enables potent silencing of drivers of in vivo growth and tumor maintenance as well as genes that sensitize GBM to radiotherapy. We find radiotherapy rewires transcriptional responses to genetic perturbations in an in vivo-dependent manner, revealing heterogenous patterns of treatment sensitization or resistance in GBM. Furthermore, we demonstrate targeting of genes that function in the tumor microenvironment, enabling alterations of ligand-receptor interactions between immune and stromal cells following in vivo CRISPRi perturbations that can affect tumor cell phagocytosis.

Conclusion: In sum, we demonstrate the utility of multiplexed perturb-seq for in vivo single-cell dissection of adult cancer and normal tissue biology across multiple cell types in the context of therapeutic intervention, a platform with potential for broad application.

Keywords: CRISPRi, CRISPR, Perturb-seq, Functional genomics, Glioblastoma, GBM, Cancer, Microenvironment, Radiotherapy

Liu *et al. Genome Biology* (2024) 25:256

Page 2 of 32

Background

Functional understanding of genes under physiological and disease states in vivo has been limited by a lack of approaches for multiplexed genetic perturbation at single-cell resolution. CRISPR functional genomics have transformed our understanding of how genetic and epigenetic perturbations impact cell types and cell states [1]. However, existing functional genomic approaches in vivo have largely focused on population averaged phenotypes, obscuring cellular heterogeneity and cell–cell interactions that are critical for multicellular biology, disease, and response to stimuli [2–6]. Coupling CRISPR screening with single-cell transcriptomics (perturb-seq) enables phenotyping of gene function using high dimensional gene expression readouts at the single-cell level [7–13]. Perturb-seq phenotypes have been used to cluster genes by shared functions into pathways, allowing identification and characterization of genes with previously unknown function, and also to map epistatic relationships between genes. The single-cell nature of perturb-seq also enables measurement of cellular heterogeneity, deconvolution of cell cycle effects, and is amenable to analysis of rare cell types. However, the majority of such efforts have focused on gene function in vitro [7–9, 11], utilize ex vivo perturbations [14, 15], or have been limited to developmental disorders [16, 17]. As tissues and organs are comprised of numerous cell types that share physical and paracrine interactions, all while being influenced by the immune system, vasculature, and tissue architecture [18, 19], single-cell transcriptomic screening using perturb-seq is especially warranted in vivo.

To establish an in vivo perturb-seq platform for multiplex interrogation of diseased or normal cells, we focused on glioblastoma (GBM), the most common primary malignant brain tumor [20]. GBM is incurable and exhibits remarkable cellular, genetic, and epigenetic heterogeneity [21, 22]. GBM cells exist in multiple interchangeable cellular states [21, 23] embedded within an immunosuppressive microenvironment [24–26], and GBM cultures in vitro do not adequately reflect the heterogeneity and dynamics of in vivo tumors [27]. Radiotherapy is the most effective adjuvant treatment for GBM, yet these tumors almost always recur [28–32]. Therefore, improved treatments for GBM are necessary as well as strategies for enhancing the efficacy of standard of care therapies such as radiotherapy. Therefore, accurate functional genomics investigations of GBM as well as other solid malignancies compel the use of in vivo models.

Here, we iteratively developed a platform for in vivo perturb-seq in malignant and normal cells in the tumor microenvironment using convection enhanced delivery (CED), a technique that exploits bulk flow kinetics for enhanced delivery of viral vectors [33, 34]. We demonstrate that transcriptomic phenotypes of oncogenic drivers can be defined in GBM malignant cells using perturb-seq, initially in cultures and then in orthotopic allografts. When combined with radiotherapy, CED perturb-seq reveals how radiotherapy treatment of established tumors rewires transcriptional responses to genetic perturbations. Furthermore, we demonstrate this platform allows for interrogation of cellular interactions between different cell types present in the tumor microenvironment upon genetic perturbation, highlighting the utility of perturbing cells in their intact environment.

Liu *et al. Genome Biology*　　(2024) 25:256

Page 3 of 32

Results

Syngeneic GBM tumors enable modeling of radiotherapy response and identification of oncogenic drivers

To begin to establish in vivo perturb-seq in tumor models with intact tumor immune microenvironments, we first utilized the GBM model GL261, which could model human tumors as well as be developed for CRISPRi loss of function screening to nominate candidates for further investigation using perturb-seq (Fig. 1A). The GL261 allograft is a well-established model that mimics aggressive human GBM with tumor features that include invasive growth, neovascularization, and orthotopic tumor formation with an intact immune system [35–37]. GL261 cells transplanted into the striata of C57BL/6 mice established tumors, and treatment with fractionated radiotherapy (RT, 2 Gy × 5 daily fractions) prolonged survival of GL261 allografts ($p = 0.0009$, log-rank test) (Fig. 1B), consistent with the known efficacy but non-curative nature of radiotherapy in this model [38], and more broadly in GBM. We then generated a GL261 cell line expressing CRISPRi machinery (dCas9-KRAB). To nominate genes that modulate GBM tumorigenesis and cellular responses to radiotherapy, we then performed large-scale CRISPRi screens in these cells in vitro against 5,234 cancer related and/or druggable genes [39], in the presence or absence of radiotherapy (2 Gy × 5 daily fractions). We identified 230 genes modifying cell growth under control conditions (negative growth hits) and 49 genes modifying radiation resistance/sensitivity (Fig. 1C, Additional file 1: Fig. S1A-B, Table S1). Gene ontology analysis of negative growth hits revealed enrichment for cell cycle, proteasome, and DNA replication genes, while radiation sensitizing hits revealed enrichment for non-homologous end joining, homologous recombination, and Fanconi anemia pathways (Fig. 1D, Additional file 1: Fig. S1C). Internally controlled growth assays validated the phenotypes of 5 growth hits and 4 radiation sensitizing hits,
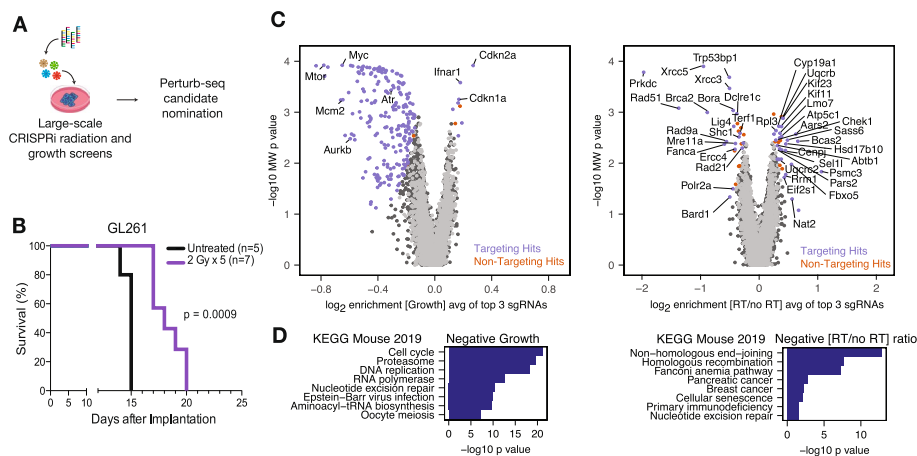
Fig. 1 CRISPRi screens identify oncogenic drivers and modifiers of radiotherapy response in GBM. **A** Schematic of in vitro screen workflow to nominate candidates for perturb-seq. **B** Kaplan–Meier survival curves of GL261 intracranial tumor models treated with either fractionated radiotherapy (2 Gy × 5 fractions) to the whole brain or no treatment. *p* value derived from log-rank test. **C** Volcano plot of log2 enrichment for the top 3 sgRNAs corresponding to each gene target in the growth (left) or radiation to growth ratio (right) phenotypes in GL261 cells. A discriminant threshold score of 7 was used for both screen analyses to nominate hit genes for in vivo perturb-seq. MW = Mann-Whitney *U*. **D** Gene ontology enrichment analysis for negative growth (left) and negative radiation to growth ratio (right) screen hits identified in **C**

Liu *et al. Genome Biology*   (2024) 25:256

Page 4 of 32

demonstrating that our CRISPRi screening data effectively nominates genes of interest in the GL261 GBM model (Additional file 1: Fig. S1D).

In vitro perturb-seq against oncogenic drivers and modifiers of radiotherapy response

To further characterize the functions of genes identified in the CRISPRi screens that regulate cell growth and radiotherapy response, we selected 48 hit genes to be further characterized by perturb-seq in GL261 cells grown in vitro (Fig. 2A). The top two sgRNAs (based on CRISPRi screen phenotypes) targeting each gene were cloned into dual sgRNA lentivirus vectors [40], and a lentivirus pool containing this library and negative control sgRNAs was transduced at an MOI of ~ 0.1 in GL261 cells stably expressing dCas9-KRAB. For in vitro perturb-seq, cultures were FACS sorted for sgRNA+ cells, treated with either fractionated radiotherapy (2 Gy $\times$ 5) or no treatment (0 Gy), and then harvested for scRNA-seq with direct capture of sgRNA tags [10]. As anticipated, sgRNA+ cells predominantly expressed two sgRNAs, with a small fraction of cells expressing four sgRNAs, reflective of cells infected by two lentiviral infection events or cell doublets (Additional file 1: Fig. S2A; the " Methods" section). Nonetheless, the total sgRNA UMI counts in the vast majority of cells were equivalent to the UMI counts from the expected sgRNA A and sgRNA B targeting each gene (Additional file 1: Fig. S2B). Only cells expressing the correct dual sgRNA vector were retained for further analysis, yielding a total of 8257 cells across two replicates for each treatment condition (Additional file 1: Fig. S2C,D). As CRISPRi silences genes through transcriptional repression, we quantified the strength of gene silencing in cells pseudobulked by sgRNA identity and revealed 88.2% and 83.3% median target gene repression in the no treatment and radiotherapy conditions, respectively (Fig. 2B). Differential expression analysis revealed 17 target genes with greater than 100 differentially expression genes (adjusted p value < 0.05 and log2 fold change magnitude > 0.1) in the absence of radiotherapy (Additional file 1: Fig. S2E). In the presence of radiotherapy, 8 gene targets passing quality control yielded greater than 100 differentially expressed genes, when internally normalized to irradiated cells expressing non-targeting control sgRNAs (Additional file 1: Fig. S2E). This pattern of differential gene expression changes was observed even after normalizing for differences in sgRNA coverage within each perturbation (Additional file 1: Fig. S2F).

We then quantified transcriptomic phenotypes for each CRISPRi genetic perturbation using differential gene expression analysis followed by gene set enrichment analysis (the " Methods" section; Fig. 2C). Perturbation of 35 target genes in the absence of radiotherapy resulted in significant alteration (adjusted p value < 0.05) in at least one gene module (Fig. 2C). We observed expected changes for genetic perturbations known to be closely or causally annotated with specific gene modules. For example, the MTORC1 Signaling gene module was downregulated the most by perturbation of *Mtor*, while perturbation of *Myc* significantly downregulated MYC Targets V1 and V2 (Fig. 2C). Hierarchical clustering of perturbations revealed grouping by screen phenotypes, gene ontology of the target, and module alterations. For instance, positive growth hits *Cdkn1a*, *Cdkn2a*, and *Rad21* clustered together and were characterized by increased MYC Target, G2M Checkpoint, and E2F Target gene expression (Fig. 2C). Mitochondrial localized Complex III components *Uqcrb* and *Uqcrc2* clustered together, as did *Atr* and its downstream target *Chek1*. Despite different molecular functions, *Kif11* and *Ifnar1* clustered together

Liu *et al. Genome Biology*   (2024) 25:256

Page 5 of 32
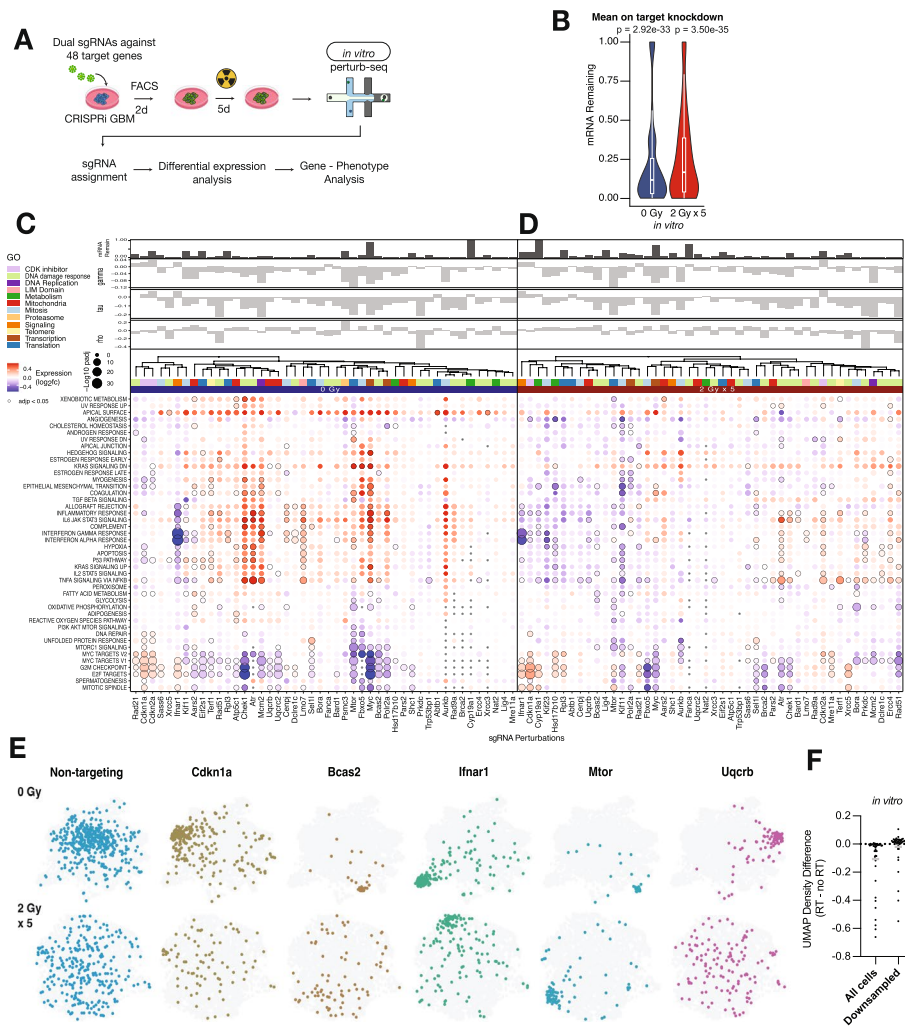
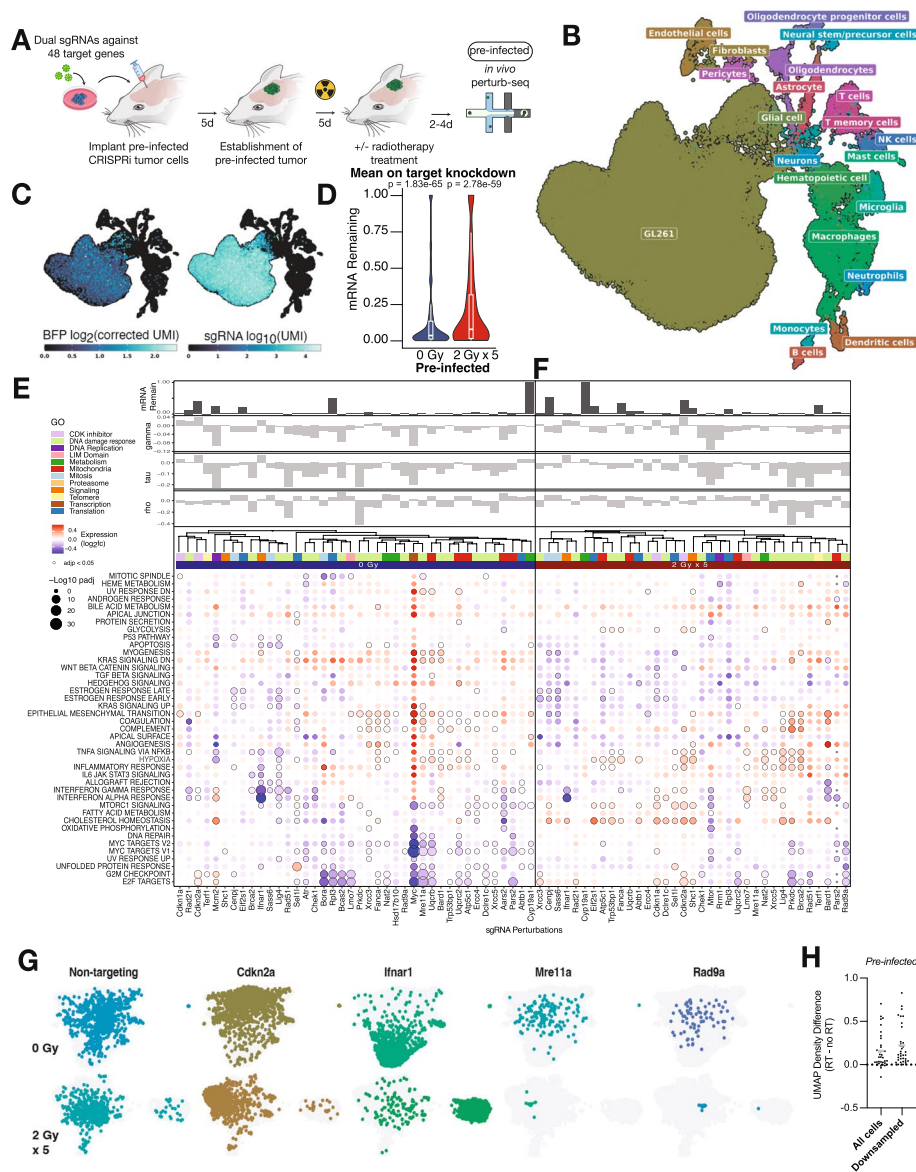**Fig. 2** In vitro perturb-seq against oncogenic drivers and modifiers of radiotherapy response in GBM cells. **A** Schematic of in vitro perturb-seq workflow against target genes nominated by genome-scale CRISPRi screens, combined with treatment with or without 2 Gy × 5 fractions of radiotherapy. **B** Distribution of mean on-target knockdown levels for all in vitro perturbations in either treatment condition. Box plots show 1st quartile, median, and 3rd quartile; whiskers represent 1.5 inter-quartile range. *p* values indicate Mann–Whitney *U* test compared to non-targeting controls. **C** Bubble plot of gene set enrichment analyses of gene expression modules (rows) following sgRNA perturbations (columns) without radiotherapy. Expression represents log$_2$ fold change normalized to non-targeting controls. Top bar charts show mRNA remaining of target gene, growth (gamma), radiation (tau), and radiation to growth ratio (rho) in vitro screen phenotypes. Gene ontology of perturbed target genes indicated. **D** As in **C** but in radiotherapy conditions. Perturbation phenotypes were normalized to irradiated cells expressing non-targeting sgRNAs. **E** LDA UMAP plots showing distribution of single cells expressing the indicated sgRNAs in either no radiotherapy (top) or radiotherapy (bottom) conditions. Cells which express sgRNAs other than the one highlighted in color are indicated in gray. **F** Difference in UMAP gaussian kernel densities between perturbations in radiotherapy (RT) and no treatment (no RT) conditions. Each point represents a particular genetic perturbation. Gray bar = mean

based on significant downregulation of interferon α, interferon γ, and TNFα signaling, revealing convergent inflammatory responses from divergent population-based screen phenotypes (Fig. 2C).

Liu *et al. Genome Biology* (2024) 25:256

Page 6 of 32

To then define the molecular alterations induced by genetic perturbations in the context of radiotherapy, we quantified transcriptomic phenotypes of the same perturbations in GL261 cell cultures treated with fractionated radiotherapy (2 Gy × 5) (Fig. 2D). When internally normalized to irradiated cells expressing non-targeting control sgRNAs, regulators of DNA damage response (e.g., *Brca2*, *Ercc4*, *Lig4*, *Mre11a*, *Prkdc*), mitosis (e.g., *Bora*), and metabolism (e.g., *Hsd17b10*, *Cyp19a1*) exhibited more pathway alterations compared to the same perturbations in the absence of radiotherapy (Fig. 2D). In contrast to CRISPRi perturbations alone, certain perturbations in the context of radiotherapy such as *Myc*, *Atr*, and *Chek1* did not produce high magnitude expression changes in interferon/inflammatory responses or the p53 pathway (Fig. 2D). We therefore asked whether radiotherapy dominated the phenotypes of cells receiving combination genetic perturbation and radiotherapy by normalizing expression profiles with those of non-targeting sgRNA-expressing cells from unirradiated cultures. These gene expression changes demonstrated homogenous upregulation of inflammatory response (47 perturbations, adjusted p value < 0.05), apoptosis (30 perturbations, adjusted p value < 0.05), and downregulation of MYC Targets V2 (37 perturbations, adjusted p value < 0.05), and therefore radiotherapy in vitro potentially masks heterogeneity in molecular functions for genes that modify radiotherapy response (Additional file 1: Fig. S2G). Consistent with this finding, linear discriminant analysis (LDA) revealed clustering of single cells by perturbations with distinct phenotypes in UMAP space, whereas single cells were more broadly distributed with the addition of radiotherapy (Fig. 2E). UMAP densities for perturbed cells were lower in radiotherapy conditions, even after normalizing for cell coverage by downsampling to equal numbers of cells in radiotherapy and no radiotherapy conditions for each perturbations (Fig. 2F).

In vivo perturb-seq against oncogenic drivers and modifiers of radiotherapy response

Glioblastoma cells are generally more resistant to radiotherapy in vivo than in vitro [41], likely due to multiple tumor-specific factors that cannot be easily recapitulated in vitro [21, 42]. To define the molecular pathways underlying oncogenic drivers and radiotherapy response in GBM, we established an in vivo perturb-seq platform in GL261 cells by transducing cells ex vivo with sgRNA libraries prior to in vivo tumorigenesis (hereafter referred to as in vivo pre-infected perturb-seq) (Fig. 3A). A GFP-tagged dual sgRNA lentivirus library targeting the same 48 genes from perturb-seq in vitro was transduced into GL261 dCas9-KRAB cell cultures, which were puromycin selected for sgRNA expression, and then transplanted intracranially into C57BL/6 mice. Tumors were allowed to expand for 5 days and were then treated with fractionated radiotherapy (2 Gy × 5) or no treatment (0 Gy), followed by single-cell dissociation and scRNA-seq with direct capture of sgRNA tags [10]. GFP-sorted cells as well as unsorted tissue dissociates were processed to capture the full extent of cellular heterogeneity. Twenty distinct stromal or immune microenvironment cell types were identified based on transcriptomic profiles, in addition to GL261 malignant cells, which were readily identified by mRNA expression of BFP (CRISPRi marker) and sgRNAs (Fig. 3B,C, Additional file 1: Fig. S3A). As was observed for in vitro perturb-seq, sgRNA+ cells predominantly expressed two sgRNAs (Additional file 1: Fig. S3B), and the total sgRNA UMIs were equivalent to the UMI counts from the expected sgRNA A and sgRNA B targeting each gene (Additional file 1:

Liu *et al. Genome Biology*   (2024) 25:256

Page 7 of 32

Fig. 3 In vivo perturb-seq against oncogenic drivers and modifiers of radiotherapy response using pre-infected GL261 cells. **A** Schematic of in vivo pre-infected perturb-seq workflow against target genes nominated by large scale CRISPRi screens, combined with treatment with or without 2 Gy × 5 fractions of radiotherapy. **B** Integrated scRNA-seq UMAP of malignant and stromal/microenvironment cells from orthotopic tumors containing pre-infected GL261 cells, including sorted and unsorted cells. **C** Integrated scRNA-seq UMAP from **B** overlayed with BFP (marker for dCas9-KRAB; left) or sgRNA (right) expression levels. **D** Distribution of mean on-target knockdown levels for all in vivo pre-infected perturbations in either treatment condition. Box plots show 1st quartile, median, and 3rd quartile; whiskers represent 1.5 inter-quartile range. *p* values indicate Mann–Whitney *U* test compared to non-targeting controls. **E** Bubble plot of gene set enrichment analyses of gene expression modules (rows) following sgRNA perturbations (columns) without radiotherapy for in vivo pre-infected perturb-seq. Expression represents log$_2$ fold change normalized to non-targeting controls. Top bar charts show mRNA remaining of target gene, growth (gamma), radiation (tau), and radiation to growth ratio (rho) in vitro screen phenotypes. Gene ontology of perturbed target genes indicated. **F** As in **E** but in radiotherapy conditions. Perturbation phenotypes were normalized to cells from irradiated tumors that expressed non-targeting sgRNAs. **G** LDA UMAP plots showing distribution of single cells from in vivo pre-infected experiments expressing the indicated sgRNAs in either no radiotherapy (top) or radiotherapy (bottom) conditions. Cells which express sgRNAs other than the one highlighted in color are indicated in gray. **H** Difference in UMAP gaussian kernel densities between perturbations in radiotherapy (RT) and no treatment (no RT) conditions. Each point represents a particular genetic perturbation. Gray bar = mean

Liu *et al. Genome Biology*   (2024) 25:256

Page 8 of 32

Fig. S3C). 30,878 in vivo GL261 cells expressing both expected sgRNAs for each gene target were identified across biological triplicate experiments from no radiotherapy or radiotherapy conditions (Additional file 1: Fig. S3D,E). Analysis of CRISPRi knockdown revealed 96.5% and 92.2% median target gene repression in the no treatment and radiotherapy conditions, respectively (Fig. 3D).

We then generated perturbation-phenotype maps using differential gene expression analysis (the " Methods" section), revealing 24 target genes with greater than 100 differentially expressed genes (adjusted *p* value < 0.05 and log2 fold change magnitude > 0.1) in the absence of radiotherapy and 34 with radiotherapy (normalized to non-targeting sgRNA in radiotherapy conditions) (Additional file 1: Fig. S3F). The increased number of differentially expressed genes in the radiotherapy conditions was observed after normalizing for sgRNA coverage per perturbation (Additional file 1: Fig. S3G). Perturbation of 40 and 30 target genes passing quality control filters resulted in significant alteration (adjusted *p* value < 0.05) in at least one gene module in the absence or presence of radiotherapy, respectively (Fig. 3E, F). Our analysis of gene module alterations in the absence of radiation demonstrated expected biology. For example, the MYC Targets V2 gene module was downregulated the most by perturbation of *Myc*, while interferon and inflammatory pathways were downregulated the most by perturbation of *Ifnar1* (Fig. 3E). Surprisingly, perturbation of certain genes with radiation sensitizing CRISPRi screen phenotypes, such as *Mre11a*, *Fanca*, and *Ercc4*, exhibited significant gene modules alterations even in the absence of radiotherapy in vivo (Fig. 3E), an observation that was not seen from in vitro perturb-seq (Fig. 2C) despite adequate coverage of these perturbations in both experimental contexts (Additional file 1: Fig. S2D, S3E). These data underscore the importance of in vivo functional interrogation of genes discovered from more traditional in vitro approaches.

We then analyzed gene module alterations induced by genetic perturbations in GL261 in vivo tumors that were treated with radiotherapy. A cluster of perturbations targeting genes involved in DNA damage response (*Xrcc5*, *Lig4*, *Prkdc*, *Brca2*, *Mre11a*, *Rad51*) exhibited radiotherapy-dependent upregulation of hypoxia and inflammatory response (Fig. 3F), while other genes with radiotherapy sensitizing phenotypes such as *Bard1* showed decreases in interferon α and interferon γ response. Consistent with these findings, perturbation of *Bard1* decreased secretion of multiple cytokines, including MCP-1 (*p* = 0.041, Student's *t* test), MIP-1α (*p* = 0.033), MIP-1β (*p* = 0.016), and TNFα (*p* = 0.026), measured by in vitro cytokine profiling assays (Additional file 1: Fig. S3H, Table S3). Similarly, perturbation of *Ifnar1* decreased secretion of these cytokines, in addition to VEGF (*p* = 0.029). In contrast, perturbation of *Atr* resulted in increased secretion of both IFNγ and VEGF (*p* = 0.0233, two-way ANOVA). Cholesterol metabolism was significantly upregulated (adjusted *p* value < 0.05) in 15 perturbations in the context of radiotherapy, compared to 3 in the absence of radiotherapy (Fig. 3E, F). These pathway alterations suggest that radiotherapy rewires the transcriptional responses to loss of genes that regulate oncogenic function or radiation responses in GBM (Fig. 3F). These radiotherapy-dependent phenotypes were also evident in LDA UMAP space (Fig. 3G). Despite expected depletion of cells expressing sgRNAs against DNA repair factors such as *Mre11a* or *Rad9a* in radiotherapy conditions, the increase in UMAP density observed for cells perturbed in the context of radiotherapy was maintained even after

Liu *et al. Genome Biology*   (2024) 25:256

Page 9 of 32

controlling for cell counts (Fig. 3H). While in vivo pre-infected perturb-seq revealed many in vivo- and radiotherapy-dependent phenotypes, one limitation of this approach is the relatively low coverage of perturbations with strong negative growth phenotypes, which precluded analysis of critical gene targets such as *Mtor* or *Aars2* in the radiotherapy conditions (Additional file 1: Fig. S3E).

Convection enhanced delivery enables in vivo perturb-seq after tumor establishment

To enable single-cell CRISPR screening in tumor cells genetically perturbed within their native physiologic context, we established in vivo perturb-seq using convection enhanced delivery (CED) to deliver sgRNA lentiviruses directly into orthotopic GBMs (Fig. 4A). We transplanted GL261 GBM cells stably expressing CRISPRi machinery (dCas9-KRAB) into the striata of C57BL/6 mice (Additional file 1: Fig. S4A). Following tumor establishment, lentiviral dual-sgRNA libraries targeting the 48 genes nominated from in vitro CRISPRi screens (Fig. 1) and also targeted in in vitro *pre-infected* perturb-seq (Figs. 2A, 3A), plus non-targeting controls were delivered to intracranial tumors using CED. Animals were treated with either cranial fractionated radiotherapy (2 Gy $\times$ 5 daily fractions) or no treatment (0 Gy). Tumors were then microdissected, dissociated, sorted for sgRNA+ cells, and harvested for scRNA-seq with direct capture of sgRNA tags [10]. Integration of FACS sorted sgRNA positive cells and sgRNA negative cells from unsorted populations revealed 22 immune, stromal, and malignant cell populations across UMAP space (Fig. 4B; Additional file 1: Fig. S4B). Analysis of sgRNA UMI counts confirmed single lentivirus vector integration events, as total sgRNA UMI counts were highly correlated with the sum of sgRNA UMI counts from sgRNA A and sgRNA B (Pearson $R = 1.00$) (Additional file 1: Fig. S4C-E). Nearly all sgRNA positive cells were GL261 malignant cells, and 2153 in vivo GL261 cells expressing only the expected dual sgRNA vectors were retained (5 pooled animals per condition-replicate) (Fig. 4C, D, Additional file 1: Fig. S4F, G). In contrast to in vivo perturb-seq experiments using pre-infected cells, CED perturb-seq allowed better recovery of sgRNAs targeting essential genes such as *Myc* and *Mtor*, thus enabling transcriptional phenotyping of genes important in tumor maintenance (Additional file 1: Fig. S4F). Analysis of CRISPRi knockdown efficacy revealed 95.5% and 95.6% median target gene repression in the no treatment and radiotherapy conditions, respectively (Fig. 4E).

We then quantified transcriptomic phenotypes for each CRISPRi genetic perturbation following CED using differential expression analysis (the " Methods" section), revealing 8 targets that passed quality and coverage filters with greater than 100 differentially expressed genes (adjusted p value < 0.05 and log2 fold change magnitude > 0.1) in the absence of radiotherapy and 15 with radiotherapy (Additional file 1: Fig. S4H). The increased number of differentially expressed genes in the radiotherapy conditions was observed after normalizing for sgRNA coverage for each perturbation (Additional file 1: Fig. S4I). Perturbation of 38 and 26 target genes passing quality control filters resulted in significant alteration (adjusted p value < 0.05) in at least one gene module in the absence or presence of radiotherapy, respectively (Fig. 4F, G). In the absence of radiotherapy, as was observed for in vitro perturb-seq (Fig. 2C) and pre-infected perturb-seq (Fig. 3E), MTORC1 Signaling was downregulated the most by perturbation of *Mtor* via CED, and perturbation of *Myc* significantly downregulated MYC Targets V1 and V2 (Fig. 4F).
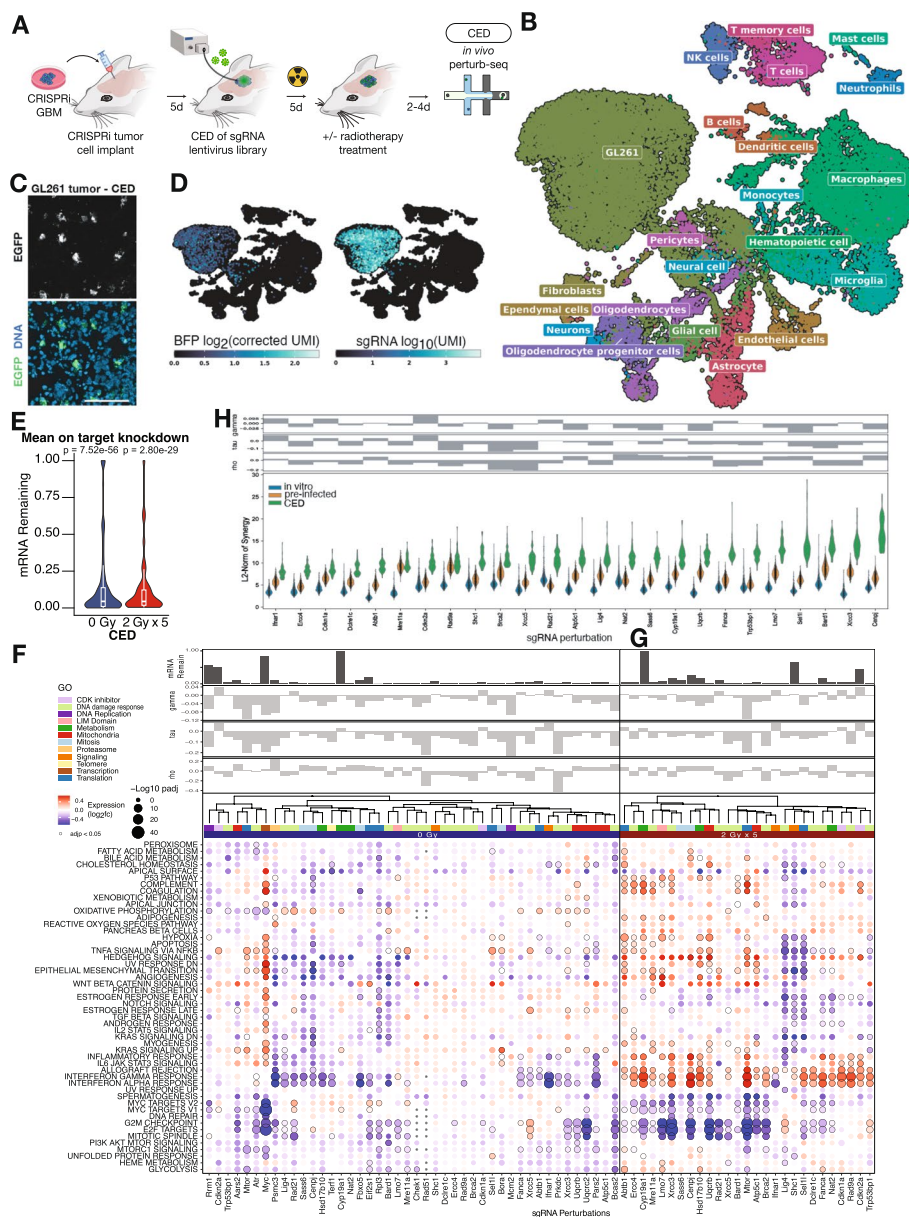
Fig. 4 In vivo perturb-seq after tumor establishment using convection enhanced delivery. **A** Schematic of in vivo CED perturb-seq workflow against target genes nominated by genome-scale CRISPRi screens, combined with treatment with or without 2 Gy × 5 fractions of radiotherapy. **B** Integrated scRNA-seq UMAP of malignant and stromal/microenvironment cells from orthotopic GL261 tumors following CED, including sorted and unsorted cells. **C** Confocal image of GL261 orthotopic tumor transduced with a sgRNA library tagged with EGFP. Scale bar, 100 µm. **D** Integrated scRNA-seq UMAP of malignant and stromal/microenvironment cells from **B** overlaid with BFP (marker for dCas9-KRAB; left) or sgRNA (right) expression levels. **E** Distribution of mean on-target knockdown levels for all in vivo CED perturbations in either treatment condition. Box plots show 1st quartile, median, and 3rd quartile; whiskers represent 1.5 inter-quartile range. *p* values indicate Mann–Whitney *U* test compared to non-targeting controls. **F** Bubble plot of gene set enrichment analyses of gene expression modules (rows) following sgRNA perturbations (columns) without radiotherapy for in vivo CED perturb-seq. Expression represents log$_2$ fold change normalized to non-targeting controls. Top bar charts show mRNA remaining of target gene, growth (gamma), radiation (tau), and radiation to growth ratio (rho) in vitro screen phenotypes. Gene ontology of perturbed target genes indicated. **G** As in **E** but in radiotherapy conditions. Perturbation phenotypes were normalized to cells from irradiated tumors that expressed non-targeting sgRNAs following CED. **H** L2-norm synergy scores for each sgRNA perturbation across all experimental contexts (in vitro, in vivo pre-infected, in vivo CED)

Hierarchical clustering of gene expression changes caused by perturbations demonstrated multiple clusters which are distinguished by which gene modules were altered, or by the known functions of the target genes (Fig. 4F). While in vitro growth screen phenotypes in the absence of radiotherapy correlated with the clustering of many perturbations, in vivo transcriptional responses were in some cases shared despite opposing screen phenotypes in vitro (Fig. 4F). For example, *Ifnar1* perturbation downregulated interferon and inflammatory signaling, as did perturbation of *Lig4* or *Rad21*, which play roles in DNA damage response and show opposing phenotypes in growth screens compared to *Ifnar1* (Fig. 4F, Table S1). In contrast, perturbation of *Atr* resulted in upregulation of interferon responses, while perturbation of *Myc* upregulated STAT3/5 signaling in CED experiments (Fig. 4F). *Atr*, *Myc*, and *Mtor* perturbations were also characterized by shared downregulation of oxidative phosphorylation genes (Fig. 4F). Mitochondrial components (*Uqcrb*, *Uqcrc2*, *Pars2*, *Atp5c1*) clustered together as well.

We then analyzed CED perturbations in the context of in vivo cranial radiotherapy. Normalized to non-targeting sgRNAs in radiotherapy conditions, heterogenous alterations in gene expression modules were observed in radiotherapy conditions (Fig. 4G). In contrast to perturbations without radiotherapy, CED perturbations in the presence of radiotherapy exhibited upregulation of inflammatory/interferon signaling, as well as activation of p53 pathway, even after normalizing to cells from the same irradiated tumors that express non-targeting sgRNAs (Fig. 4G). Analysis of transcriptional death programs revealed that, in addition to p53 activation, ferroptosis drivers [43] were significantly (adj. $p < 0.05$) upregulated following perturbation of *Trp53bp1*, and the apoptosis gene expression module was significantly dysregulated (adj. $p < 0.05$) across 7 perturbation-treatment combinations (Additional file 1: Fig. S5A).

Given known mutations in *Kras* and *p53* within the GL261 model of GBM [38], we asked whether the Ras or p53 signaling pathways could be associated with transcriptional modules such as those involving STAT3 or STAT5. Gene set enrichment analysis of perturbations revealed covarying alterations between Ras signaling and STAT3 as well as STAT5 signaling modules that were positively correlated, albeit weakly (Pearson $R = 0.135$, $R = 0.179$, respectively) (Additional file 1: Fig. S5B). We then asked whether differentially expressed genes following perturbations could be associated with STAT3 transcription factor binding activity. We integrated ChIP-seq data mapping STAT3 binding sites within a mouse model of GBM [44], and we quantified for each perturbation-treatment condition the proportion of differentially expressed genes whose promoter regions (defined as 0–2 kb upstream the transcriptional start site) contained one or more STAT3 ChIP-seq peaks. Nine perturbations in the radiotherapy condition and 4 perturbations in the no radiotherapy condition were associated with a significant proportion ($p < 0.05$, Fisher's exact test) of differentially expressed genes containing STAT3 binding sites (Additional file 1: Fig. S5C). Furthermore, perturbations in the radiotherapy condition were more likely to be associated with STAT3 binding sites above the genomic background compared to perturbations in the no radiotherapy condition ($p = 0.00013$, Fisher's exact test).

Multiple clusters of perturbations were observed following hierarchical clustering of in vivo perturbations, and these gene expression profiles spanned classes of transcriptomic alterations characterized by (1) low proliferative, low inflammatory, and low

Liu *et al. Genome Biology*   (2024) 25:256

Page 12 of 32

epithelial mesenchymal transition genes (*Sel1l*, *Lig4*, *Shc1*), (2) low proliferative and high inflammatory signaling (e.g., *Cyp19a1*, *Xrcc3*, *Cenpj*, *Mtor*, *Atp5c1*, *Brca2*, *Fanca*), and (3) variable proliferative and high inflammatory signaling (e.g., *Rad9a*, *Trp53bp1*, *Cdkn1a*, *Cdkn2a*). Perturbations from each of these classes demonstrated radiotherapy-dependent phenotypes, as evidenced by preferential aggregation of cells with perturbations such as *Ercc4*, *Fanca*, and *Shc1* in LDA UMAP space with radiotherapy (Additional file 1: Fig. S6A, B). As was the case for pre-infected perturb-seq (Fig. 3H) (but not in vitro perturb-seq (Fig. 2F)), UMAP density was greater for CED perturbations combined with radiotherapy (Additional file 1: Fig. S6C).

Given that in vivo perturbations rewired transcriptional responses following radiotherapy, we asked whether perturbations combined with radiotherapy could be modeled as a linear combination of perturbation effects in the absence of radiotherapy and radiotherapy effects alone, with potential for synergy. We used CINEMA-OT (causal independent effect module attribution with optimal transport) [45] to quantify synergy scores, defined as the difference between the observed phenotype for combination treatment and the predicted phenotype assuming a linear additive relationship between genetic perturbation and radiotherapy. Synergy scores were greater for the majority of perturbations with CED compared to either in vitro or pre-infected contexts (Fig. 4H). In vitro CRISPRi screen phenotypes for radiation overlayed with the synergy metric showed little correlation (Fig. 4H), demonstrating the utility of in vivo CED perturb-seq to reveal the roles of radiation sensitizing and resistance gene targets in vivo.

Convection enhanced delivery enables in vivo perturb-seq within the tumor microenvironment

As cancers comprise both malignant and non-malignant host cells of the stroma or immune microenvironment, we asked whether in vivo CED perturb-seq could be applied toward stromal or immune microenvironment cells in GBM tumors. To that end, we used the SB28 syngeneic mouse GBM model, which is driven by *Nras* overexpression and establishes a myeloid cell-rich tumor immune microenvironment similar to human GBM [46, 47]. Although both GL261 and SB28 form orthotopic tumors in immunocompetent animals, SB28 tumors harbor a dearth of T cells and resistance to immunotherapy that are more reflective of human GBM [48]. SB28 cells that did not express CRISPRi machinery were transplanted intracranially into immunocompetent mice constitutively expressing dCas9-KRAB [49], enabling cell type-selective sgRNA stabilization and knockdown of genes in microenvironment cells but not in malignant cells (Fig. 5A). Target genes (*Apoe*, *C1qa*, *Cd44*, *Cd74*, *Lyz2*, *Ptprc*) were selected for perturbation based on cell type-specific expression or function in the myeloid lineage, given their importance in GBM pathogenesis and potential for therapeutic intervention [50, 51]. We delivered a lentiviral sgRNA library (3 individual sgRNAs targeting each of 6 target gene, including a non-targeting sgRNA) by CED into SB28 tumors, dissected tumors 5 days following CED, and performed scRNA-seq with direct sgRNA capture of both FACS sorted and unsorted tumors. Analysis revealed a diversity of non-cancer cell types (e.g., macrophages, astrocytes, endothelial cells) within the tumor microenvironment, existing alongside SB28 cancer cells, which were readily distinguishable by *Nras* overexpression (Fig. 5B, D, Additional file 1: Fig. S7,S8A). Consistent with their high abundance
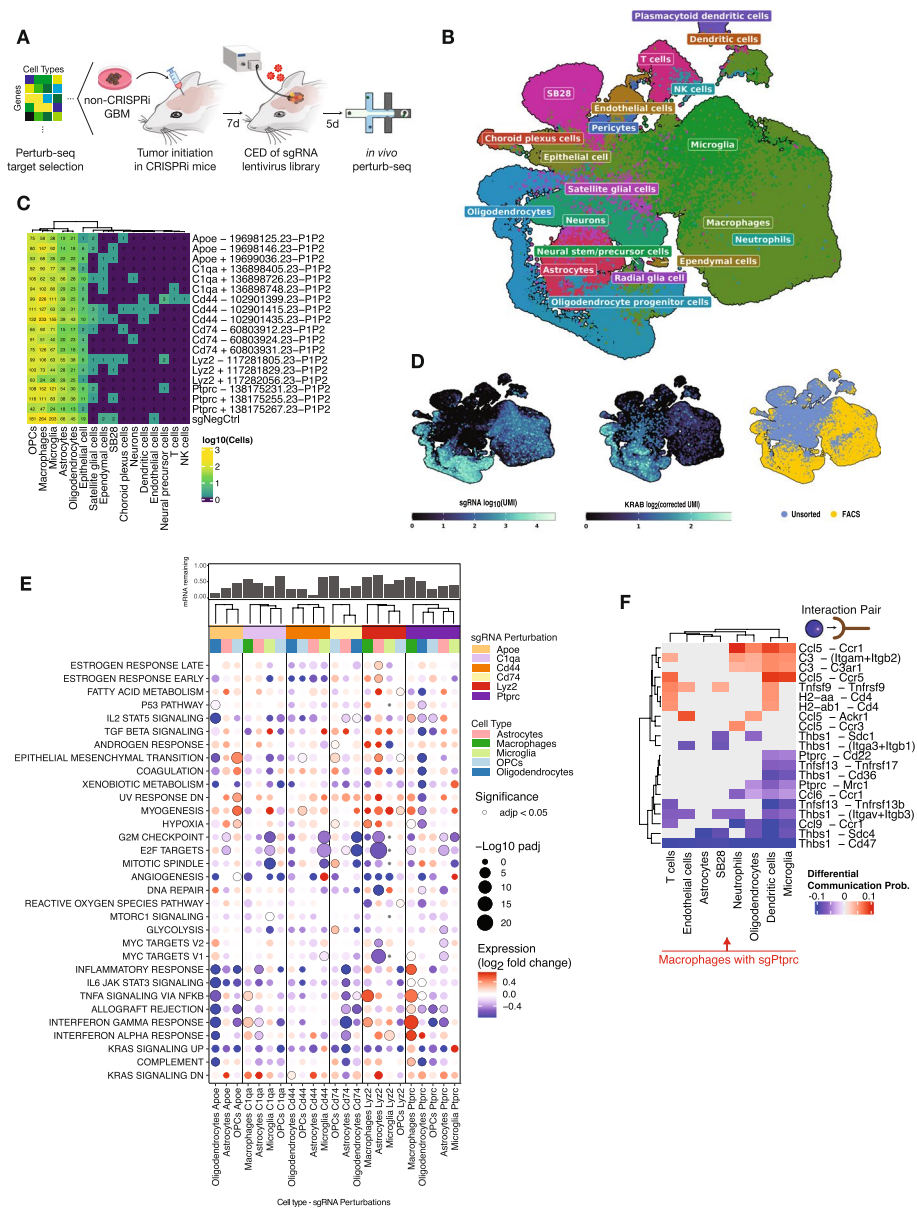
Fig. 5 In vivo perturb-seq in tumor microenvironment cells. **A** Schematic of in vivo CED perturb-seq in orthotopic SB28 GBM allograft models against target genes. **B** Integrated scRNA-seq UMAP of malignant and stromal/microenvironment cells from orthotopic SB28 tumors following sgRNA delivery using CED. **C** Number of sgRNA positive cells for each sgRNA perturbation across cell types identified in **B**. **D** Integrated scRNA-seq UMAP of malignant and stromal/microenvironment cells from **C** overlaid with sgRNA UMI (left), KRAB expression level (middle), or whether the single cells were FACS sorted (right). **E** Bubble plot of gene set enrichment analyses of gene expression modules (rows) following sgRNA perturbations (columns) spanning cell types identified in **C**. Expression represents log$_2$ fold change normalized to non-targeting controls from the same cell type. mRNA remaining refers to target gene. **F** Differential communication probabilities for ligand-receptor interactions inferred from transcriptional profiles of perturbed macrophages (either negative control or *Ptprc* sgRNA) along with target cells of the tumor microenvironment within the same SB28 tumors

in SB28 allografts, macrophages, microglia, and glial cells represented the large majority of sgRNA-expressing cells in these tumors, spanning 6909 FACS-sorted cells from quadruplicate experiments (Fig. 5C, D). Integrated UMAP analysis of unsorted SB28 and GL261 tumors from CED perturb-seq experiments demonstrated a combined total

Liu *et al. Genome Biology*   (2024) 25:256

Page 14 of 32

of 27 cell type clusters and that SB28 orthotopic tumors contained greater proportions of macrophages and microglia, while having fewer CD4+T cells compared to GL261 tumors (Additional file 1: Fig. S8B-D), consistent with prior reports [46]. Analysis of CRISPRi knockdown levels revealed heterogeneous target gene suppression across the different cell types analyzed in this experiment, and only sgRNAs with greater than 30% knockdown (less than 70% mRNA remaining) were retained for subsequent analysis in each cell type (Additional file 1: Fig. S9A).

Quantification of transcriptomic phenotypes for each CRISPRi genetic perturbation following CED in cell types with sufficient sgRNA coverage—macrophages, microglia, astrocytes, oligodendrocytes, oligodendrocyte progenitor cells (OPCs)—revealed cell type-dependent gene module alterations (Fig. 5E). We then investigated the consequences of perturbing the phosphatase *Ptprc* in macrophages in vivo, given its proinflammatory phenotype spanning multiple gene modules, which were not observed after perturbing this same target in other cell types (Fig. 5E). *Ptprc* knockdown resulted in upregulation of genes associated with interferon α and interferon γ response, as well as IL2/STAT5 and TNFα signaling (Fig. 5E), consistent with the role of *Ptprc* in innate immunity and cytokine signaling [52, 53]. To determine if genetic perturbation could influence cell–cell interactions within SB28 intracranial tumors, we identified putative cell–cell interactions using CellChat [54] (the " Methods" section). Perturbation of *Ptprc*, *Lyz2*, *C1qa*, or *Cd44* resulted in altered frequencies of cell–cell interactions between innate (i.e., macrophages and microglia) and adaptive immune cells (i.e., T cells and NK cells) (Additional file 1: Fig. S9B), suggesting that genetic perturbations could affect interactions between different cell types. We then quantified the pairwise differences in communication probabilities in macrophages following *Ptprc* suppression and other cell types, versus macrophages expressing non-targeting control sgRNAs and other cell types. Following *Ptprc* knockdown, *Ccl5–Ccr1/3/5* interactions increased with immune and stromal cell types (Fig. 5F), reflective of the overall proinflammatory phenotype of *Ptprc* knockdown in macrophages (Fig. 5E). In contrast, *Ptprc* knockdown in macrophages also abrogated cell–cell interactions through suppression of *Thbs1*, *Ccl6*, *Ccl9*, and *Ptprc* itself, reducing communication probabilities between macrophages and dendritic cells, microglia, SB28 malignant cells, among other cell types (Fig. 5F). To test whether *Ptprc* loss in macrophages affects critical immune cell functions, we performed in vitro time lapse microscopy phagocytosis assays by co-culturing *Ptprc* Cas9 loss of function macrophages with Ramos lymphoma cells, a type of cancer cell that is sensitive to antibody-dependent cellular phagocytosis [55] (Fig. 6A, B). *Ptprc* knockdown in J774 macrophages significantly reduced the degree of antibody-dependent cellular phagocytosis of malignant cells, proportional to the degree of *Ptprc* suppression ($p=0.0015$, sgPtprc-1; $p=0.0302$, sgPtprc-2; two-way ANOVA) (Fig. 6C, D). These results not only reveal the role of *Ptprc* as a regulator of paracrine and direct interactions within tumors but also demonstrate that non-cancer cell types present in the tumor microenvironment can be perturbed and then phenotyped using our in vivo CED perturb-seq approach.

Liu *et al. Genome Biology*   (2024) 25:256

Page 15 of 32
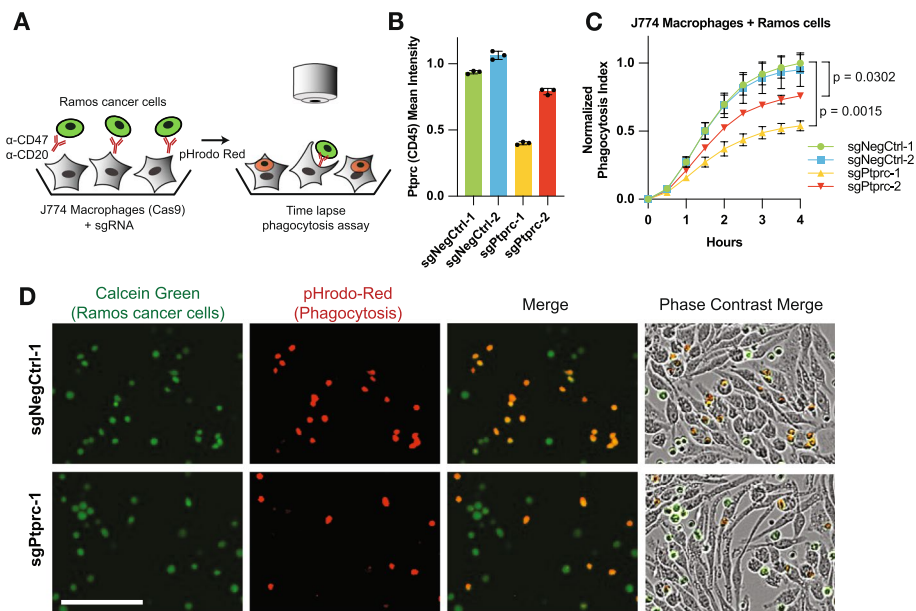
Fig. 6 *Ptprc* loss attenuates macrophage phagocytosis of malignant cells. **A** Schematic of time lapse microscopy assays for co-cultured J774 macrophages (*Ptprc* knockdown or control) and Ramos lymphoma cells. pHrodo red intracellular indicator dye is used to measure extent of phagocytosis following opsonization of malignant cells with α-CD47 and α-CD20 antibodies. **B** Distribution of mean *Ptprc* (CD45) expression measured by flow cytometry. $n = 3$ replicates. **C** Phagocytosis time lapse microscopy assay for uptake of Ramos cancer cells by J774 macrophages. *p* values, two-way ANOVA comparing each *Ptprc* perturbation to both negative control sgRNAs. $n = 3$ cell culture wells. **C** Images of J774 macrophages with indicated genotypes co-cultured with pHrodo red-labelled malignant Ramos cells after 4 h incubation. Scale bar, 100 μm. Representative of two independent experiments performed in biological triplicate wells

Discussion

Multiplex in vivo perturbations coupled with measurement of rich transcriptional phenotypes can reveal genotype–phenotype relationships in normal and disease contexts that would not be feasible in cell cultures. Here, we developed a platform for in vivo perturb-seq to interrogate the function of oncogenic drivers and treatment response mechanisms in GBM, a fatal brain malignancy. Using iterative progression of in vitro target gene nomination, in vivo transplantation of in vitro infected malignant tumor cells, to direct delivery of sgRNA cargo using CED, we demonstrate that functional genomic screens performed in vivo reveal distinct phenotypic alterations spanning a diversity of cell autonomous and non-cell autonomous transcriptional pathways. In vivo CED perturb-seq also reveals how radiotherapy treatment of established tumors rewires transcriptional responses to genetic perturbations. Furthermore, this platform allows for interrogation of cellular interactions in the tumor microenvironment, highlighting the utility of perturbing cells that exist in their intact environment. Targeting sgRNA payloads directly into orthotopic tumors complements existing strategies of CRISPR/Cas9 perturbations in vivo, including Cre-Lox [5, 56–58] and Tet-inducible [59, 60] methods. Direct tumor targeting via CED has the added advantage of circumventing leakiness associated with inducible systems [61], the potential for temporally and spatially controlled genetic perturbations, multiplexing large pools of perturbations, and the ability to rapidly adapt CRISPR screens toward various disease models without the need for

Liu *et al. Genome Biology*   (2024) 25:256

Page 16 of 32

complex genetic engineering. Furthermore, the use of CED for in vivo genetic screens could facilitate the translation of genetic perturbations as a therapeutic strategy, as CED is clinically used as a promising treatment approach for unresectable brain tumors [62]. While CED provides unique advantages for delivery to the central nervous system, including bypassing the blood brain barrier [33], similar sustained intratumoral delivery strategies could be advantageous for genetic screens in other tumors such as pancreatic or prostate cancer [63–65].

The observation that in vivo perturbations resulted in greater heterogeneity of transcriptional responses, especially when combined with radiotherapy, was a distinct feature of performing perturbations within a preformed tumor with an intact immune system. However, we cannot exclude contributions from differences in the experimental timelines between in vitro and in vivo perturb-seq workflows, as in vivo experimental timelines were constrained by slower growth rates of tumors compared to their respective cell cultures [66], therefore requiring longer periods of time between perturbation and cell isolation. Despite these caveats, we have shown that cytokine alterations that were measured in vivo using a longer timeline (i.e., 19 days) were consistent with in vitro cytokine production measured on a shorter timeline (i.e., 7 days) (Additional file 1: Fig. S3H). Furthermore, the apparent discrepancy between the cell types transduced by sgRNA lentiviruses in the GL261 CED experiments for CRISPRi in malignant cells (Fig. 4D, Additional file 1: Fig. S4G) compared to the SB28 CED experiments for CRISPRi in the microenvironment cells (Fig. 5B, D) may be due to absence or presence of CRISPRi machinery, which is known to stabilize and substantially prolong the half-life of sgRNAs [67]. As such, the SB28 microenvironment experiments, which utilized animals that expressed H11-dCas9-KRAB in each normal cell, enabled recovery of sgRNAs in multiple glial and immune cell types (Fig. 5B, D). CRISPRi activity in the microenvironment cells also appeared less efficacious than in GBM malignant cells (Additional file 1: Fig. S7B). This is likely a consequence of using computationally predicted sgRNAs for the microenvironment perturbations rather than sgRNAs nominated based on screen scores from genome-scale CRISPRi screens, which were feasible for cultured GBM cells (Fig. 1A, B). In future work, sgRNA nomination for perturb-seq could be performed entirely in vivo, thereby maximizing the likelihood of discovering in vivo specific phenotypes using highly active sgRNAs. Such efforts could be enabled by expanding or modifying the in vivo tropism of sgRNA libraries through adeno-associated viruses or virus-like particles [17, 68].

Conclusions

In conclusion, in vivo CED perturb-seq, which we have iteratively developed, enables multiplex interrogation of complex biological processes in cancer and non-cancer cell types. This platform reveals mechanisms of treatment responses in GBM, and it also serves as the foundation for simultaneous discovery and characterization of therapeutic vulnerabilities that are uniquely functional in vivo.

Liu *et al. Genome Biology*   (2024) 25:256

Page 17 of 32

Methods

In vitro CRISPRi screens, analysis, and validation

HEK-293 T cells were cultured in Dulbecco's Modified Eagle Medium (Gibco, #11,960,069) supplemented with 10% fetal bovine serum (FBS) (Life Technologies, #16,141). Cell cultures were authenticated by STR analysis at the UC Berkeley DNA Sequencing Facility as well as routinely tested for mycoplasma using the MycoAlert Detection Kit (Lonza, #75,866–212). GL261 cells were cultured in Dulbecco's Modified Eagle Medium (Gibco, #11,960,069) supplemented with 10% fetal bovine serum (FBS) (Life Technologies, #16,141), and GL261 cells stably expressing the CRISPR interference (CRISPRi) machinery dCas9-KRAB were generated as previously described [69, 70]. Lentivirus was produced from transfected HEK293T cells with packaging vectors (pMD2.G #12,259, Addgene, and pCMV-dR8.91, Trono Lab) following the manufacturers protocol (#MIR6605, Mirus). GL261 GBM cells were transduced with lentivirus harboring SFFV-dCas9-BFP-KRAB, and the top ~ 25% of cells expressing BFP were FACS sorted, expanded, and FACS sorted a second time.

For genome-scale CRISPRi screening in vitro, we used a mouse sgRNA library [39] comprising 27,300 sgRNAs targeting 5234 cancer-related and/or druggable genes, in addition to 530 non-targeting control sgRNAs. Pooled lentivirus was generated as above, and GL261 cells were transduced using spin-infection of viral supernatant of a MOI of ~ 0.1 at 1000 g for 120 min. Four days of puromycin selection (1.5 μg/mL) was performed, followed by 2 days of growth in non-puromycin 10% FBS in DMEM media. Two replicates of each screen were performed at a coverage of $525 \times$ cells per sgRNA, in both no radiation and radiation (2 Gy $\times$ 5 fractions delivered every other day) treatment conditions. Infection efficiency was evaluated by measuring GFP positivity on flow cytometry. Initial (T0) cell populations were then frozen in 10% DMSO and processed for genomic DNA using the NucleoSpin Blood XL Kit (Machery-Nagel, #740,950.50). Endpoint cell pellets were harvested for genomic DNA after 12 days of growth, corresponding to ~ 7 and ~ 5 doublings in the no radiation and radiation conditions, respectively. sgRNA sequencing libraries were prepared using NEBNext Ultra II Q5 PCR MasterMix (New England Biolabs, #M0544L) and sequenced on an Illumina NextSeq-500 as previously described [59].

sgRNAs with fewer than 100 reads at T0 were removed from subsequent analysis. Enrichment or depletion of sgRNA abundances were determined by downsampling trimmed sequencing reads to equivalent amounts across all samples. Growth phenotype (gamma) was defined as log2(sgRNA count T12 (0 Gy)/sgRNA count T0) minus median sgNTC log2(sgRNA count T12 (0 Gy)/sgRNA count T0), then normalized by the number of cell doublings, as previously described [69]. Radiation phenotype (tau) was defined as log2(sgRNA count T12 (2 Gy $\times$ 5)/sgRNA count T0) minus median sgNTC log2(sgRNA count T12 (2 Gy $\times$ 5)/sgRNA count T0), then normalized by the number of cell doublings in the radiation screen. Radiation to growth ratio phenotype (rho) was defined as log2(sgRNA count T12 (2 Gy $\times$ 5)/sgRNA count T12 (0 Gy)). Gene-level phenotypes were summarized as the mean of the top 3 sgRNAs against a given gene, ranked according to screen phenotype. Statistical significance was calculated using the Mann–Whitney *U* test for a given perturbation compared to the sgRNA distribution of the non-targeting control sgRNAs (Table S1). A discriminant threshold of 7, derived

Liu *et al. Genome Biology*   (2024) 25:256

Page 18 of 32

from the product of normalized gene phenotype and -log10(*p*-value), corresponding to an empiric false discovery rate of ~2%, was selected for hit definitions [69]. To ascertain the fidelity of our mouse cell CRISPRi screens, we overlapped gamma phenotypes (without radiotherapy treatment) in our GL261 screens with gamma phenotypes from K562 CRISPRi cells subjected to genome-wide human CRISPRi growth screens [69]

Internally controlled competitive growth assays were then performed to validate CRISPRi screen hits. GL261 cultures were partially transduced with sgRNA expression lentiviruses with a GFP tag (Addgene 187241) [40], and the percentage of sgRNA positive cells were measured over time using flow cytometry, in the presence or absence of radiotherapy (2 Gy × 5 fractions).

Cytokine profiling assays

GL261 cells expressing dCas9-KRAB were transduced with lentivirus at an MOI of ~0.1 and were subjected to puromycin selection (1.0 μg/μL) for 3 days, starting 2 days after transduction, followed by 2 days of growth in non-puromycin recovery media. Supernatant (1 mL) was harvested from biological triplicate cell cultures and clarified by centrifuge twice at 3000 g for 5 min at 4C. Five hundred microliters of supernatant per sample were profiled using the Mouse Cytokine/Chemokine 32-Plex Discovery Assay Array (Eve Technologies). The multiplexing analysis was performed using the Luminex™ 200 system (Luminex, Austin, TX, USA) by Eve Technologies Corp. (Calgary, Alberta). Thirty-two markers were simultaneously measured in the samples using Eve Technologies' Mouse Cytokine 32-Plex Discovery Assay® (MilliporeSigma, Burlington, MA, USA) according to the manufacturer's protocol. The 32-plex consisted of Eotaxin, G-CSF, GM-CSF, IFNγ, IL-1α, IL-1β, IL-2, IL-3, IL-4, IL-5, IL-6, IL-7, IL-9, IL-10, IL-12(p40), IL-12(p70), IL-13, IL-15, IL-17, IP-10, KC, LIF, LIX, MCP-1, M-CSF, MIG, MIP-1α, MIP-1β, MIP-2, RANTES, TNFα, and VEGF. Assay sensitivities of these markers range from 0.3 to 30.6 pg/mL for the 32-plex. Cytokines that were not detected or out of standard curve range in all conditions were omitted from analysis. Cytokines were row normalized for visualization. Significance was calculated using unpaired two-sample Student's *t*-test for comparison of individual cytokines between perturbations and negative controls and two-way ANOVA across triplicate samples for comparisons of individual perturbations across multiple cytokines.

Intracerebral tumor establishment

Five to 6-week-old female C57BL/6 (Envigo Laboratories, Livermore, CA), housed under aseptic conditions, received intracranial tumor cell injection as previously described [71] and as approved by the University of California San Francisco Institutional Animal Care and Use Committee. For the microenvironment perturb-seq, mice expressing dCas9-KRAB from the H11 locus with a mCherry tag (JAX # 030000) were utilized. Briefly, mice were anesthetized by combination of intraperitoneal injection of a mixture containing ketamine (100 mg/kg) and xylazine (10 mg/kg) and inhalation of isoflurane. The scalp was surgically prepped, and a skin incision ~10 mm in length was

made over the middle frontal to parietal bone. The surface of the skull was exposed so that a small hole was made 3.0 mm to the right of the bregma and just in front of the coronal suture with a 25-gauge needle. A 26-gauge needle attached to a Hamilton syringe was inserted into the hole in the skull. The needle was covered with a sleeve that limits the injection depth to 3–4 mm. Three microliters of tumor cell suspension (300,000 GL261 cells; 30,000 SB28 cells) was injected into the right caudate putamen at a rate of 1 µL/min by free hand. The skull surface was then swabbed with hydrogen peroxide before the hole was sealed with bone wax to prevent reflux. The scalp was closed with surgical staples.

Bioluminescence imaging of intracranial tumor growth

For bioluminescence imaging (BLI), mice were anesthetized with inhalation of isoflurane, then administered 150 mg/kg of luciferin (D-luciferin potassium salt, Gold Biotechnology, St. Louis, MO) via intraperitoneal injection. Ten minutes after luciferin injection, mice were examined for tumor bioluminescence with an IVIS Lumina imaging station and Living Image software (Caliper Life Sciences, Alameda, CA), and intracranial regions of interest were recorded as photons per second per steradian per square cm [71].

Convection enhanced delivery of lentivirus

Convection enhanced delivery was performed as previously described [72]. Infusion cannulas were constructed with silica tubing (Polymicro Technologies, Phoenix, AZ) fused to a 0.1-ml syringe (Plastic One, Roanoke, VA) with a 0.5-mm stepped tip needle that protruded from the silica guide base. The use of the stepped design has been shown to increase the rate and volume of delivery through CED, as well as reduce the amount of reflux, thereby maximizing broad, targeted, and controlled distribution of infused agents toward the tumor [73]. The syringe was loaded with 15 µL concentrated lentivirus produced using the LV-MAX Lentiviral Production System (Thermo Fisher #A35684) according to manufacturer's protocol, followed by $200 \times$ concentration using ultracentrifuge (Beckman L8-80 M) at 25,000 g for 2.5 h at 4 °C. Concentrated lentivirus was tested for in vitro titers and achieved $1-2 \times 10^9$ TU/mL. Animals were anesthetized with a combination of intraperitoneal injection of a mixture containing ketamine (100 mg/kg) and xylazine (10 mg/kg) and inhalation of isoflurane. The puncture hole used for intracranial tumor establishment (described above) was identified at surface of the skull 3.0 mm to the right of the bregma and just in front of the coronal suture. The Hamilton syringe was attached to a microinfusion pump (Bioanalytical Systems, Lafayette, Ind.), and the syringe with silica cannula was lowered through the puncture hole made in the skull [71, 74], targeting the same region in the caudate putamen where tumor cells had been previously injected. The concentrated lentivirus was infused at a rate of 1 µL/min until a volume of 15 µL had been delivered. Cannulas were removed 2 min after completion of infusion. The skull surface was then swabbed with hydrogen peroxide before the hole was sealed with bone wax to prevent reflux. The scalp was closed with surgical staples.

Whole brain animal irradiation

Mice were anesthetized by combination of intraperitoneal injection of a mixture containing ketamine (100 mg/kg) and xylazine (10 mg/kg) and inhalation of 2.5% isoflurane with 1 L of oxygen per minute for 5 min prior to being positioned on an irradiation platform located 16.3 cm from a Cesium-137 source (J. L. Shepherd & Associates, San Fernando, CA). Animal subjects' eyes, respiratory tracts, and bodies were protected with lead shielding. Whole brain irradiation (2 Gy for 5 daily fractions) was delivered at a dose rate of 247 cGy/min [75]. After irradiation, animals were monitored until recovery from anesthesia. Following no radiation or radiation treatment, animals were sacrificed and brains were quickly removed from the skull, and the tumor mass was microdissected as previously described [71].

Imaging

Fluorescence microscopy was performed on a Zeiss LSM 800 confocal laser scanning microscope with Airyscan. Images were processed and quantified from at least 2 regions per condition using ImageJ9. Hematoxylin and eosin-stained slides were imaged on a Zeiss Axio Zoom V16 light microscope.

In vitro and in vivo perturb-seq in malignant cells

Perturb-seq sgRNA libraries were designed by nominating 48 genes with radiation sensitizing, radiation resistance, negative growth, or positive growth phenotypes in in vitro CRISPRi screens as described above. Protospacer sequences were selected from the optimized mouse CRISPRi v2 library [39], and the top two scoring sgRNAs for each target gene based on depletion or enrichment phenotypes were cloned into dual sgRNA lentivirus expression vectors with direct capture tags (Addgene 187241) [40] using NEBuilder HiFi DNA Assembly Master Mix (New England Biolabs #E2621L) (Table S2). Concentrated lentivirus of pooled sgRNA libraries were produced as described above.

For in vitro perturb-seq, GL261 cells expressing dCas9-KRAB were transduced with lentivirus at an MOI of ~ 0.1, and cells were FACS sorted (BD FACSAria Fusion) for GFP positivity 48 h following transduction. Cell cultures were irradiated using a Cesium-137 source to 2 Gy $\times$ 5 fractions delivered daily, starting on same day of FACS. Twelve hours following the final fraction of radiotherapy, cells were trypsinized and harvested in single-cell suspension on the 10 $\times$ Chromium Controller (10 $\times$ Genomics, #1000204). Single-cell perturb-seq libraries were processed using the Chromium Next GEM Single Cell 3′ GEM, Library & Gel Bead Kit v3.1 with Feature Barcoding (10 $\times$ Genomics, #1000269), allowing direct capture of modified sgRNAs, and sequenced on an Illumina NovaSeq-6000. In vitro perturb-seq experiments were performed in biological duplicate cultures for each treatment condition.

For pre-infected in vivo perturb-seq, GL261 cells expressing dCas9-KRAB were transduced with lentivirus at an MOI of ~ 0.1 and were subjected to puromycin selection (1.5 µg/µL) for 3 days, starting 2 days after transduction, followed by 2 days of growth in non-puromycin recovery media. Three hundred thousand cells were intracranially injected into each mouse as described above. Tumors were allowed to establish and expand for 5 days, and radiation (or no treatment) was delivered to a dose of 2 Gy $\times$ 5 daily fractions as described above. For tumors of the no radiation arm, tumor harvest

was performed 12 days following intracranial injection of cells. For tumors of the radiation arm, tumor harvest was performed 2 days following completion of radiation treatment or 14 days total after intracranial injection of cells. Harvested tumors were minced and dissociated to single-cell suspension using the Papain Dissociation System (Worthington #LK003150) following manufacturer's protocol without the use of ovomucoid protease inhibitor. Cell suspensions were passed through a 70 µm strainer (Corning, #352350), centrifuged at 300 g for 5 min, and resuspended in cold phosphate buffered saline. To capture cells of the tumor microenvironment as well as sgRNA transduced malignant cells in vivo, we processed a fraction of the dissociated tumor for immune cell depletion using CD11b MicroBeads (Miltenyi Biotec #130–097-142) following manufacturer's protocol on LS Columns, followed by FACS sorting for sgRNA positive cells tagged with GFP. Sorted cells as well as a separate fraction of the dissociated tumor that was not CD11b depleted or FACS sorted were processed for scRNA-seq with direct capture of sgRNA tags using $10 \times$ Chromium Controller ($10 \times$ Genomics, #1000204). Single-cell perturb-seq libraries were processed as described for in vitro perturb-seq. Pre-infected in vivo perturb-seq experiments were performed in biological triplicate tumors.

For CED in vivo perturb-seq, GL261 cells expressing dCas9-KRAB were intracranially injected into mice as described above. Tumors were allowed to establish and expand for 5 days, and CED of concentrated lentivirus was performed as described above. For the radiation treatment arm, whole brain irradiation was delivered to a dose of 2 Gy $\times$ 5 daily fractions as described above, initiating 2 days following CED to allow lentiviral transduction and sgRNA expression. For tumors of the no radiation arm, tumor harvest was performed 5 days following CED, for a total of 12 days following implantation of cells. For tumors of the radiation arm, tumor harvest was performed 2 days following completion of radiation treatment or 14 days total after intracranial injection of cells. Harvested tumors were minced and dissociated to single-cell suspension as described for pre-infected in vivo perturb-seq. Five tumors from biological replicate animals in each treatment arm were pooled to increase sgRNA positive cell recovery (0.7–1.1% sgRNA positive per pool by FACS). From these pools of dissociated cells, separate immune cell depletion followed by FACS sorting for GFP and unenriched populations were captured for scRNA-seq with direct capture of sgRNAs as described above. Single-cell perturb-seq libraries were processed as described for in vitro perturb-seq.

In vivo perturb-seq in tumor microenvironment cells

Microenvironment perturb-seq sgRNA libraries were designed by nominating 6 genes that were either overexpressed in myeloid cell types from scRNA-seq of SB28 orthotopic tumors or by their known gene function in the myeloid lineage. Protospacer sequences were selected from the optimized mouse CRISPRi v2 library [39] by their predicted rank order, and the top 3 sgRNAs were individually cloned into single sgRNA expression vectors with direct capture cs1 sequences (Addgene # 122238) [10] using restriction digest (BstXI and BlpI) and T4 ligation (NEB # M0202M). A non-targeting sgRNA sequence was included as well. Concentrated lentivirus of pooled sgRNA was produced as described above. SB28 cells [47] without CRISPRi machinery were intracranially injected into the H11-dCas9-KRAB mice (JAX # 030000) as described above, and CED

of concentrated lentivirus was performed as described above 7 days after tumor implantation. Five days following CED, tumors were harvested, minced, and dissociated to single-cell suspension using the Papain Dissociation System (Worthington #LK003150) following manufacturer's protocol without the use of ovomucoid protease inhibitor. Cell suspensions were passed through a 70-µm strainer (Corning, #352350), centrifuged at 300 g for 5 min, and resuspended in cold phosphate buffered saline. To capture the full spectrum of cell types including sgRNA positive and negative cells, both single-cell suspensions sorted for sgRNA positivity and lacking the SB28 GFP marker (RFP + /GFP −), and unsorted cells were processed for scRNA-seq with direct capture of sgRNA tags using 10 × Chromium Controller (10 × Genomics, #1000204). Single-cell perturb-seq libraries were processed using the Chromium Next GEM Single Cell 3′ GEM, Library & Gel Bead Kit v3.1 with Feature Barcoding (10 × Genomics, #1000269), allowing direct capture of modified sgRNAs, and sequenced on an Illumina NovaSeq-6000. Tumor microenvironment perturb-seq was performed in biological quadruplicates, with each replicate consisting of two pooled animals.

Macrophage co-culture and time lapse microscopy assays

J774 Cas9 cells (a gift from A. Sil) were cultured in Dulbecco's Modified Eagle Medium (Gibco, #11960069) supplemented with 10% heat-inactivated fetal bovine serum (FBS) (Gibco, #A5256801), 2 mM L-glutamine (Gibco, #25030164), and 100 U/mL Penicillin–Streptomycin (Gibco, #15140163) and transduced with lentiviral constructs expressing a puromycin resistance cassette, GFP, and either a negative control sgRNA or a *Ptprc*-targeting sgRNA (Table S2). Following transduction, cells were allowed to recover before selection with puromycin (5 µg/ml) for 72 h. Transduction and selection were confirmed using the GFP marker via flow cytometry. Cells were given sufficient time (> 5 days) to recover from selection before use in phagocytosis assays.

Phagocytosis assays were performed largely as previously [55]. Briefly, 10,000 J774 Cas9 macrophages expressing the indicated sgRNAs were plated in 96-well plates (Falcon, Cat. No 353072). Ramos Cas9 target cells were cultivated in RPMI 1640 medium (Gibco, #11875119) supplemented with 10% heat-inactivated fetal bovine serum (FBS) (Gibco, #A5256801), 2 mM L-glutamine (Gibco, #25030164), and 100 U/mL Penicillin–Streptomycin (Gibco, #15140163). Twenty-four hours prior to the assay, J774 cells were stimulated with 100 ng/ml LPS (Sigma, #L2880). On the day of the assay, 1 million Ramos cells were pelleted, washed twice with PBS (Gibco, #10010023), and stained with 100 nM pHrodo-Red-SE (Invitrogen, #P36600) and 333 ng/mL Calcein-AM (Invitrogen, #C1430) for 30 min in a tissue culture incubator. Cells were then pelleted, resuspended with complete DMEM, counted via flow cytometry, and diluted to a concentration of 400,000 cells/mL with complete DMEM. Anti-human CD20 (BioXCell, #SIM0008, lot no. 909923J2) and anti-human CD47 (BioXCell, #BE0019-1, lot no 878622D1) were then both added to final concentrations of 500 ng/mL. Fifty microliters of cell suspension was then added to appropriate wells.

Plates were then transferred to an incubator containing an Incucyte S3 (Sartorius) and imaged every 30 min, with 5 images taken per well. An analysis definition was created using surface-fit segmentation, a green threshold of 10 GCU (which excluded the much weaker green signal in the GFP + J774 macrophages), and a red threshold of 3 RCU,

and the total integrated red intensity within green + /red + objects (i.e., cells that were phagocytosed while alive) was determined. To calculate the normalized phagocytosis index, the signal at t0 for each condition (corresponding to a small amount of debris) was first subtracted from all timepoints, and then the signal for each well at each timepoint was divided by the average signal of the control-2 condition at the final (4 h) plotted timepoint.

CD45 depletion in J774 Cas9 macrophages was quantified by flow cytometry. One million J774 Cas9 macrophages expressing either control or *Ptprc*-targeting sgRNAs were pelleted and resuspended in 100 μL of flow staining buffer (Fisher, #501,128,916) containing anti-mouse CD16/32 (UCSF antibody core, #AM004) at a final concentration of 0.8 mg/mL for FcR blocking and incubated for 10 min at 4 ℃. The J774s were then pelleted, resuspended in 100 μL of flow staining buffer containing APC-conjugated anti-mouse CD45 (Ptprc) (Invitrogen, cat no 17−0451-82, lot no. #2,820,764) and stained for 30 min at 4 ℃ protected from light. After staining, cells were washed twice with flow staining buffer and then analyzed using an Agilent Novocyte Quanteon Flow Cytometer.

Perturb-seq computational analyses

Pre-processing, sgRNA calling, cell type identification

Library demultiplexing, gene expression read alignment to human genome GRCh38, UMI quantification, and sgRNA assignment and quantification were performed in Cell Ranger version 6.1.2 with sgRNA barcoding (10X Genomics). Single-cell RNA-seq analysis was performed in Seurat version 4.3.0 [76] in R version 4.3.1. For analysis of cellular heterogeneity across all perturb-seq experiments, including malignant cells and microenvironment, cells with greater than 200 detected features were retained. RNA expression data was transformed using SCTransform [77] in Seurat, and expression featureplots show log2 UMIs corrected by SCTransform. Expression heatmaps of scRNA-seq data show SCTransform residuals (normalized expression). Uniform manifold approximation and projection (UMAP) was performed using the Seurat function RunUMAP using the first 30 dimensions from principal component analysis of the transformed expression data, using parameters (min.dist = 0.7). Cell type identification of stromal and microenvironment cells was performed using single-cell multiresolution marker-based annotation (scMRMA) version 1.0 [78], using the PanglaoDB mouse cell types reference [79], with manual confirmation of known marker gene specificity. To deconvolve malignant tumor cells from stromal tissue with potentially similar RNA expression profiles, we integrated scRNA-seq data from our in vitro cultures and in vivo experiments to allow manual annotation of in vitro GBM cells, as these were processed in separate 10 × lanes and therefore could be distinguished by metadata. Similarly, sgRNA positive cells from the pre-infected perturb-seq experiments could be readily identified as malignant GBM cells, as these were transduced with sgRNA prior to in vivo implantation. Using these pre-defined cell clusters of malignant cells, projection of cells from the CED perturb-seq experiment onto an integrated UMAP space demonstrated a highly abundant population of cells which co-clustered with malignant cells from the pre-infected perturb-seq experiment, and therefore these cells were identified as in vivo malignant GBM cells and were therefore analyzed in the context of their corresponding non-malignant cells.

Liu *et al. Genome Biology* (2024) 25:256

Page 24 of 32

Cells were retained for further analysis if they expressed both the expected sgRNA A and sgRNA B against a given target gene, corresponding to the sgRNAs of the dual sgRNA expression vector. Cells with sgRNAs targeting multiple genes were separately analyzed for the potential of gene–gene interaction analysis. However, quantification of gene UMI count, unique gene counts, and housekeeping gene expression suggested that these multi-sgRNA vector expressing cells represented rare homotypic cell doublets that could not be readily distinguished from cells transduced with multiple sgRNA vectors using doublet detection software [80]. Therefore, these cell doublets were not retained for further analysis. Target gene knockdown was quantified by library normalizing the untransformed transcriptome UMIs of each sgRNA positive cell and obtaining the mean expression of each gene across all cells belonging to a given sgRNA within each individual GEM group. RNA remaining for each gene target was calculated by dividing the pseudobulk expression in on-target cells with cells expressing non-targeting negative control sgRNAs, with a pseudocount of 0.1 added to each component. Quantification of RNA remaining values were capped at a ceiling of 1.0. Expression featureplots were generated using SCPubr version 1.1.2 [81]. Statistics were calculated using the non-parametric Mann–Whitney U test comparing on-target mRNA remaining levels with those of non-targeting controls.

Differential gene expression analysis

First, we filtered the expression objects as follows: For each differential expression run, we isolated cells by the desired experimental context (in vitro, pre-infected, CED), selected for FACS sorted only cells in the pre-infected context, and selected cells with sgRNA expression called for both expected sgRNAs against a given target gene. We removed cells with perturbations that had coverage of less than or equal to 5 cells. Next, we used the default findDE method from the DElegate package version 1.1.0 [82] to find differentially expressed genes. DElegate is a wrapper around DESeq2 that adapts bulk sequencing methods for single-cell data. The effect of running findDE is to run DESeq2 with the Wald test on randomly assigned 3-group pseudoreplicates. findDE's input is a Seurat object and metadata specifications for a group of interest and a control group to measure against. We ran findDE comparing cells with a particular perturbation + / − radiation to the non-targeting perturbation + no radiation—a normalization scheme we call "noRTNormalized"—as well as a particular perturbation + / − radiation to the treatment-matched non-targeting perturbation + / − radiation, a normalization scheme that internally controls for whether cells received radiotherapy, we call "condNormalized." Per perturbation, findDE's output is a table that provides—for each gene expressed in the cells compared—the following information: the gene name, the average expression of the gene (using deseq:baseMean), the log2 fold change, the test statistic, the *p*-value, and the FDR adjusted *p*-value. We performed this DElegate::findDE workflow for all perturbations across the three experimental contexts—in vitro, pre-infected, and convection enhanced delivery. Each output represented a comparison of expression between perturbed cells and the control cells. Next, we screened each of the resulting results sets to find the differentially expressed genes. Within each set, we considered a gene differentially expressed if it passed DESeq2's expression filters (meaning it had a

non-NA *p*-value and FDR adjusted *p*-value), had an absolute value log2 fold change of greater than 0.1, and an adjusted *p*-value of less than 0.05.

Downsampled differential gene expression analysis

To account for differences in cell sampling between radiotherapy and no radiotherapy treatment conditions, we prepared downsampled differential expression output by modifying the preprocessing steps prior to running DElegate's findDE function. First, we removed perturbations with less than or equal to 5 cells. Then, we randomly downsampled using dplyr::sample_n the number of cells for each perturbation such that there were equal numbers of cells in the radiotherapy and no radiotherapy conditions, for each experimental context (i.e., in vitro vs. in vivo). Differential gene expression analysis was then performed as described above, and the number of differentially expressed genes in the downsampled analysis was quantified identically to the non-downsampled workflow.

Gene set enrichment analysis (GSEA)

For GSEA, we used the DESeq2 output as described above. For each perturbation x radiation condition—and thus each comparison or each CSV—we first used the annotables package (v0.2.0) to convert gene symbols to ENSEMBL v109 gene IDs. Genes that failed to convert were eliminated. We also removed genes that DESeq2 indicated did not pass independent filtering. Then, we ranked the remaining genes by their log2 fold changes and ran gene set enrichment analysis using fgsea (v1.27.1), a package for fast GSEA, and msigdbr (v7.5.1), the R implementation of the Molecular Signatures Database. We set the maximum size of allowed gene sets to 500 and set the eps parameter—which bounds the lowest *p*-value possible—to 0 to allow for arbitrarily low *p*-values.

This analysis resulted in a set of pathways for each perturbation x radiation condition, their corresponding normalized enrichment scores, and the *p*-values and adjusted *p*-values indicating significance of enrichment. We ran this analysis for both "noRTNormalized" and "condNormalized" schemes, described above. We indicated the normalized enrichment scores for all pathways that have an adjusted *p*-value lower than 0.05 in any perturbation x radiation condition.

For bubble plots, we show the mean log2 fold change, which we calculated as follows for each pathway x (perturbation x radiation) condition: first, we found the genes shared between a given pathway's msigdb gene set and the union of all differentially expressed genes with valid ENSEMBL IDs across perturbation x radiation conditions for a given normalization scheme. Then, we took the mean log2 fold change of these shared genes for each perturbation x radiation condition. Genes that did not pass DESeq quality filtering were set to have a log2 fold change of 0 prior to calculating the mean, to ensure that genes that did not pass quality filtering would have minimal contribution to the mean log2 fold changes.

Visualization of perturbation space with linear discriminant analysis

To separate perturbations in transcriptomic space, we ran linear discriminant analysis (LDA) on all perturbations for each radiotherapy/no radiotherapy condition. We

first filtered out low coverage perturbations (≤ 5 cells) and applied a centered log transformation normalization. Then, we used Seurat's [83] CalcPerturbSig function to generate perturbation signatures based on 40 principal components and the 20 nearest neighbors. Finally, we separated out cells by treatment condition and fed them into Seurat's MixscapeLDA function. We used a log2 fold change threshold of 0.1 to be consistent with our DESeq2 settings. Otherwise, we set the seed to the default value of 42 and the number of principal components to the default value of 10. For visualization, we chose a UMAP with the maximum number of linear discriminants found per condition. To perform LDA UMAP analysis with the downsampled set of cells, we first removed perturbations with less than or equal to 5 cells. Then, we randomly downsampled the number of cells for each perturbation using the R function dplyr::sample_n such that there were equal numbers of cells in the radiotherapy and no radiotherapy conditions for each experimental context. We then performed linear discriminant analysis with the same parameters as above.

To quantify density of cells in UMAP space, we calculated gaussian kernel densities for the UMAP coordinates in 2 dimensions for all (or downsampled) cells expressing a given sgRNA pair, with 10,000 total bins (100 bins in each UMAP 1/UMAP 2 dimension spanning the full range of coordinates). The maximum z density was obtained for each sgRNA target in either radiotherapy or no radiotherapy conditions, and the difference between these values was calculated.

Treatment-perturbation modeling and synergy analysis

To model interactions between perturbations and radiation treatment, we used CINEMA-OT (causal independent effect module attribution with optimal transport), a method that separates treatment and confounder effects using independent component analysis and then matches cells across treated/untreated conditions using optimal transport [45]. The matching can then be used to generate individual treatment effect matrices (ITE matrices), which indicate what a hypothetical treatment effect would be for each gene of each control cell. When multiple treatments are present, one can use the matchings to quantify a synergy score between treatments by defining a synergy matrix as $ITE(A+B) - (ITE(A) + ITE(B))$, where A and B are separate treatments. We used cinemaot.synergy in the cinemaot (v0.0.5) Python package (https://github.com/vandijklab/CINEMA-OT), to generate synergy scores per cell per gene between sgRNA perturbations and radiation. This was performed by passing in a perturbation with radiation as $A+B$, the same perturbation with no radiation as A, and radiation with a non-targeting sgRNA as B. Before running CINEMA-OT, we generated highly variable genes using scanpy's (v1.9.6) highly_variable_genes method, choosing a min_mean of 0.0125, max_mean of 3, min_disp of 0.5, max_disp of Inf, span of 0.3, and 20 bins. We then ran PCA on the highly variable genes using scanpy's [84] tl.pca method, passing in the "arpack" solver, 50 dimensions, a random state of 0, and "zero-centered," meaning PCA calculated from the covariance matrix.

CINEMA-OT itself—and thus the cinemaot.synergy method—takes in the following parameters: the number of independent components, a threshold for setting the Chatterjee coefficient for confounder separation, a parameter for setting the smoothness of entropy-regularized optimal transport, a parameter for the stop condition of OT

Liu *et al. Genome Biology*   (2024) 25:256

Page 27 of 32

convergence, and whether to return matrices weighted by the number of cells (a method termed CINEMA-OT-W). We set the number of independent components to 10, the threshold for confounder separation to 0.5, and the smoothness parameter to $1e-3$ to adjust for data sparsity. The stop condition we maintained at the default value of $1e-3$, and we did not weight by the number of cells.

We ran cinemaot.synergy for each perturbation across all experimental contexts, generating a synergy score per cell per gene—a synergy score matrix. We then calculated synergy scores per cell by summing the synergies for any gene whose absolute value (average synergy) across all cells in that perturbation was greater than the default parameter of 0.15. For visualization purposes, we then calculated the L2-norms for each cell.

Chromatin profiling analysis

To interrogate the chromatin profiles of STAT3 binding in mouse models of GBM, we analyzed ChIP-seq data mapping STAT3 binding sites within a mouse model of GBM: astrocytes expressing ectopic EGFRvIII (GEO GSM1241827) [44]. We quantified for each perturbation-treatment condition in our perturb-seq experiments, all unique differentially expressed genes (defined as genes having absolute value log2 fold changes relative to the non-targeting control greater than 0.5, with an adjusted *p*-value of less than 0.05), whose promoter regions (defined as 0–2 kb upstream the transcriptional start site) had one or more overlaps with a STAT3 ChIP-seq peak from GEO GSM1241827. Overlaps were performed using the mm9 mouse genome reference and pybedtools (v 0.10.0). The proportion of differentially expressed genes that contained one or more STAT3 peaks was then compared to the genome-wide background, defined as the proportion of all promoter regions which overlapped with a STAT3 peak. Statistical significance was calculated using the Fisher's exact test with the following 2 contingency tables: (1) whether each perturbation's genes being differentially expressed are associated with at least one STAT3 peak and (2) whether radiation treatment is associated with a frequency of STAT3-peak containing perturbations above the genome-wide background frequency. For visualization, we included normalized enrichment scores for the expression of the JAK/STAT3 pathway for each perturbation.

Microenvironment perturb-seq analysis

Preprocessing, data transformation, and UMAP analysis was performed using Cell Ranger version 6.1.2 with sgRNA barcoding (10X Genomics) followed by Seurat version 4.3.0 [76] in R version 4.3.1 as described above. For microenvironment cells, cells with greater than 200 detected features were retained. Cell types were identified by performing Louvain clustering using the first 30 dimensions from PCA space and using a resolution parameter of 0.4. Top marker genes from these clusters were queried in EnrichR [85, 86]. Unbiased cell type annotation was also performed using scMRMA as described above, with good agreement to cluster-based annotations. SB28 cells were readily identified by overexpression of *Nras* [47]. On target gene knockdown analysis was performed as described above. Integrated UMAP analysis of combined SB28 and GL261 tumors was performed by merging all unsorted SB28 and GL261 scRNA-seq data from CED perturb-seq experiments that were not subjected to radiotherapy and then performing

UMAP and cluster identification as described above. Tumor proportions were calculated based on relative cell counts belonging to each cell type identity.

For differential gene expression analysis in the microenvironment cells, instead of running DESeq independently for each radiation condition, we ran DESeq independently for each cell type. We first filtered the expression objects, removing cells with perturbations with coverage less than or equal to 5 cells or cells that do not have expression of a single sgRNA. We then ran DElegate's findDE method for each perturbation in each cell type against the non-targeting sgRNA (sgNegCtrl3). Per perturbation, we again received a CSV file that provided gene names, log2 fold changes, adjusted *p*-values, etc. Each CSV file was fed into downstream analysis. Gene set enrichment analysis was performed as described above. However, instead of running GSEA independently per radiation condition, we ran GSEA independently for each cell type.

Cell–cell interaction analysis between ligands and receptors was performed using CellChat version 1.6.1 [54], using the CellChatDB.mouse interaction database. Over-expressed genes and interactions were identified, and communication probability was determined using a truncatedMean approach with trim$=0.01$, a minimum of 5 cells per communication, without weighting of relative population size. Interactions with p value< 0.05 were retained for analysis and quantified as interaction frequencies. To calculate differential communication probabilities following a given sgRNA perturbation, we generated matrices corresponding to the difference in communication probability between perturbed and non-targeting control cells for each ligand-receptor combination across all cell types. For heatmap visualization, only ligand-receptor combinations with differential communication probabilities greater than 0.05 in magnitude in at least one cell type were retained.

Supplementary Information

The online version contains supplementary material available at https://doi.org/10.1186/s13059-024-03404-6.

Additional file 1: Supplementary Figures.

Additional file 2: Table S1. In vitro growth and radiation phenotypes from pooled CRISPRi screens in GL261.

Additional file 3: Table S2. sgRNA libraries used for in vivo perturb-seq.

Additional file 4: Table S3. Cytokine profiling assay raw data in pg/mL.

Additional file 5: Review history.

Peer review information
Kevin Pang and Andrew Cosgrove were the primary editors of this article and managed its editorial process and peer review in collaboration with the rest of the editorial team.

Review history
The review history is available as Additional file 5.

Authors' contributions
All authors contributed substantially to the inception, design, implementation, analysis, or writing of this report. All authors approved the manuscript. SJL, LG, DRR, WW, TO, and RAK designed the study and analyses. Experiments were performed by SJL, CZ, JP, AM, DP, TCC, KS, TO'L, TO, DRR, and LG. Computational data analyses were performed by SJL, CZ, AB, and DW. The study was supervised by SJL, DL, TO, RAK, MSB, WW, DRR, and LG. The manuscript was prepared by SJL, LG, and CZ with input from all authors.

Availability of data and materials

All sequencing data have been deposited on NCBI SRA accession number PRJNA1005229 [87]. Computational code, including output for perturb-seq differential expression analyses, has been deposited under the open source Apache License, Version 2.0, on GitHub at https://github.com/GilbertLabUCSF/gbm_perturb and archived on Zenodo [88] at the time of publication.

Declarations

Ethics approval and consent to participate

The study was approved by the University of California San Francisco Institutional Animal Care and Use Committee.

Consent for publication

Not applicable.

Competing interests

The authors declare no competing interests.

Author details

[1]Department of Radiation Oncology, University of California San Francisco, San Francisco, CA 94143, USA. [2]Department of Neurological Surgery, University of California San Francisco, San Francisco, CA 94143, USA. [3]Arc Institute, Palo Alto, CA 94304, USA. [4]Department of Anatomy, University of California San Francisco, San Francisco, CA 94143, USA. [5]Department of Pathology, University of California San Francisco, San Francisco, CA 94143, USA. [6]Biological and Medical Informatics Graduate Program, University of California San Francisco, San Francisco, CA 94143, USA. [7]Departments of Pediatrics, Neurology, and Helen Diller Family Comprehensive Cancer Center, University of California, San Francisco, CA 94143, USA. [8]Department of Urology, University of California San Francisco, San Francisco, CA 94143, USA. [9]Department of Neuroscience, Icahn School of Medicine, Mount Sinai, New York, NY 10029, USA.

References

1. Przybyla L, Gilbert LA. A new era in functional genomics screens. Nat Rev Genet. 2022;23:89–103.
2. Beronja S, Janki P, Heller E, Lien W-H, Keyes BE, Oshimori N, et al. RNAi screens in mice identify physiological regulators of oncogenic growth. Nature. 2013;501:185–90.
3. Miller TE, Liau BB, Wallace LC, Morton AR, Xie Q, Dixit D, et al. Transcription elongation factors represent in vivo cancer dependencies in glioblastoma. Nature. 2017;547:355–9.
4. Chow RD, Guzman CD, Wang G, Schmidt F, Youngblood MW, Ye L, et al. AAV-mediated direct in vivo CRISPR screen identifies functional suppressors in glioblastoma. Nat Neurosci. 2017;20:1329–41.
5. Platt RJ, Chen S, Zhou Y, Yim MJ, Swiech L, Kempton HR, et al. CRISPR-Cas9 knockin mice for genome editing and cancer modeling. Cell. 2014;159:440–55.
6. Chen S, Sanjana NE, Zheng K, Shalem O, Lee K, Shi X, et al. Genome-wide CRISPR screen in a mouse model of tumor growth and metastasis. Cell. 2015;160:1246–60.
7. Adamson B, Norman TM, Jost M, Cho MY, Nuñez JK, Chen Y, et al. A multiplexed single-cell CRISPR screening platform enables systematic dissection of the unfolded protein response. Cell. 2016;167:1867-1882.e21.
8. Dixit A, Parnas O, Li B, Chen J, Fulco CP, Jerby-Arnon L, et al. Perturb-Seq: dissecting molecular circuits with scalable single-cell RNA profiling of pooled genetic screens. Cell. 2016;167:1853-1866.e17.
9. Datlinger P, Rendeiro AF, Schmidl C, Krausgruber T, Traxler P, Klughammer J, et al. Pooled CRISPR screening with single-cell transcriptome readout. Nat Methods. 2017;14:297–301.
10. Replogle JM, Norman TM, Xu A, Hussmann JA, Chen J, Cogan JZ, et al. Combinatorial single-cell CRISPR screens by direct guide RNA capture and targeted sequencing. Nat Biotechnol. 2020;38:954–61.
11. Replogle JM, Saunders RA, Pogson AN, Hussmann JA, Lenail A, Guna A, et al. Mapping information-rich genotype-phenotype landscapes with genome-scale Perturb-seq. Cell. 2022;185:2559-2575.e28.
12. Norman TM, Horlbeck MA, Replogle JM, Ge AY, Xu A, Jost M, et al. Exploring genetic interaction manifolds constructed from rich single-cell phenotypes. Science. 2019;365:786–93.
13. Liu SJ, Casey-Clyde T, Cho NW, Swinderman J, Pekmezci M, Dougherty MC, et al. Epigenetic reprogramming shapes the cellular landscape of schwannoma. Nat Commun. 2024;15:476.
14. Lara-Astiaso D, Goñi-Salaverri A, Mendieta-Esteban J, Narayan N, Valle CD, Gross T, et al. In vivo screening characterizes chromatin factor functions during normal and malignant hematopoiesis. Nat Genet. 2023;55(9):1542–54
15. Dhainaut M, Rose SA, Akturk G, Wroblewska A, Nielsen SR, Park ES, et al. Spatial CRISPR genomics identifies regulators of the tumor microenvironment. Cell. 2022;185(7):1223–1239.e20
16. Jin X, Simmons SK, Guo A, Shetty AS, Ko M, Nguyen L, et al. In vivo Perturb-Seq reveals neuronal and glial abnormalities associated with autism risk genes. Science. 2020;370:eaaz6063.
17. Santinha AJ, Klingler E, Kuhn M, Farouni R, Lagler S, Kalamakis G, et al. Transcriptional linkage analysis with in vivo AAV-Perturb-seq. Nature. 2023;622(7982):367–75.
18. Kuhn M, Santinha AJ, Platt RJ. Moving from in vitro to in vivo CRISPR screens. Gene Genome Ed. 2021;2:100008.
19. Hanahan D. Hallmarks of cancer: new dimensions. Cancer Discov. 2022;12:31–46.

20. Ostrom QT, Price M, Neff C, Cioffi G, Waite KA, Kruchko C, et al. CBTRUS statistical report: primary brain and other central nervous system tumors diagnosed in the United States in 2016–2020. Neuro-Oncol. 2023;25:iv1-99.
21. Neftel C, Laffy J, Filbin MG, Hara T, Shore ME, Rahme GJ, et al. An integrative model of cellular states, plasticity, and genetics for glioblastoma. Cell. 2019;178(4):835–849.e21
22. Venteicher AS, Tirosh I, Hebert C, Yizhak K, Neftel C, Filbin MG, et al. Decoupling genetics, lineages, and microenvironment in IDH-mutant gliomas by single-cell RNA-seq. Science. 2017;355:eaai8478.
23. Bhaduri A, Lullo ED, Jung D, Müller S, Crouch EE, Espinosa CS, et al. Outer radial glia-like cancer stem cells contribute to heterogeneity of glioblastoma. Cell Stem Cell. 2020;26:48-63.e6.
24. Hara T, Chanoch-Myers R, Mathewson ND, Myskiw C, Atta L, Bussema L, et al. Interactions between cancer cells and immune cells drive transitions to mesenchymal-like states in glioblastoma. Cancer Cell. 2021;39:779-792.e11.
25. Antunes ARP, Scheyltjens I, Duerinck J, Neyns B, Movahedi K, Ginderachter JAV. Understanding the glioblastoma immune microenvironment as basis for the development of new immunotherapeutic strategies. eLife. 2020;9:e52176.
26. Ravi VM, Neidert N, Will P, Joseph K, Maier JP, Kückelhaus J, et al. T-cell dysfunction in the glioblastoma microenvironment is mediated by myeloid cells releasing interleukin-10. Nat Commun. 2022;13:925.
27. Lee J, Kotliarova S, Kotliarov Y, Li A, Su Q, Donin NM, et al. Tumor stem cells derived from glioblastomas cultured in bFGF and EGF more closely mirror the phenotype and genotype of primary tumors than do serum-cultured cell lines. Cancer Cell. 2006;9:391–403.
28. Walker MD, Alexander E, Hunt WE, MacCarty CS, Mahaley MS, Mealey J, et al. Evaluation of BCNU and/or radiotherapy in the treatment of anaplastic gliomas. A cooperative clinical trial. J Neurosurg. 1978;49:333–43.
29. Stupp R, Mason WP, van den Bent MJ, Weller M, Fisher B, Taphoorn MJB, et al. Radiotherapy plus concomitant and adjuvant temozolomide for glioblastoma. N Engl J Med. 2005;352:987–96.
30. Stupp R, Hegi ME, Mason WP, van den Bent MJ, Taphoorn MJB, Janzer RC, et al. Effects of radiotherapy with concomitant and adjuvant temozolomide versus radiotherapy alone on survival in glioblastoma in a randomised phase III study: 5-year analysis of the EORTC-NCIC trial. Lancet Oncol. 2009;10:459–66.
31. Stupp R, Taillibert S, Kanner A, Read W, Steinberg DM, Lhermitte B, et al. Effect of tumor-treating fields plus maintenance temozolomide vs maintenance temozolomide alone on survival in patients with glioblastoma: a randomized clinical trial. JAMA. 2017;318:2306–16.
32. Perry JR, Laperriere N, O'Callaghan CJ, Brandes AA, Menten J, Phillips C, et al. Short-course radiation plus temozolomide in elderly patients with glioblastoma. N Engl J Med. 2017;376:1027–37.
33. Jahangiri A, Chin AT, Flanigan PM, Chen R, Bankiewicz K, Aghi MK. Convection-enhanced delivery in glioblastoma: a review of preclinical and clinical studies. J Neurosurg. 2017;126:191–200.
34. Bankiewicz KS, Eberling JL, Kohutnicka M, Jagust W, Pivirotto P, Bringas J, et al. Convection-enhanced delivery of AAV vector in parkinsonian monkeys; in vivo detection of gene expression and restoration of dopaminergic function using pro-drug approach. Exp Neurol. 2000;164:2–14.
35. Candolfi M, Curtin JF, Nichols WS, Muhammad AKMG, King GD, Pluhar GE, et al. Intracranial glioblastoma models in preclinical neuro-oncology: neuropathological characterization and tumor progression. J Neuro-Oncol. 2007;85:133–48.
36. Haddad AF, Young JS, Amara D, Berger MS, Raleigh DR, Aghi MK, et al. Mouse models of glioblastoma for the evaluation of novel therapeutic strategies. Neuro-Oncol Adv. 2021;3:vdab100-.
37. Ausman JI, Shapiro WR, Rall DP. Studies on the chemotherapy of experimental brain tumors: development of an experimental model. Cancer Res. 1970;30:2394–400.
38. Szatmári T, Lumniczky K, Désaknai S, Trajcevski S, Hídvégi EJ, Hamada H, et al. Detailed characterization of the mouse glioma 261 tumor model for experimental glioblastoma therapy. Cancer Sci. 2006;97:546–53.
39. Horlbeck MA, Gilbert LA, Villalta JE, Adamson B, Pak RA, Chen Y, et al. Compact and highly active next-generation libraries for CRISPR-mediated gene repression and activation. eLife. 2016;5:914.
40. Replogle JM, Bonnar JL, Pogson AN, Liem CR, Maier NK, Ding Y, et al. Maximizing CRISPRi efficacy and accessibility with dual-sgRNA libraries and optimal effectors. eLife. 2022;11:e81856.
41. Taghian A, duBois W, Budach W, Baumann M, Freeman J, Suit H. In vivo radiation sensitivity of glioblastoma multiforme. Int J Radiat OncolBiolPhys. 1995;32:99–104.
42. Dirkse A, Golebiewska A, Buder T, Nazarov PV, Muller A, Poovathingal S, et al. Stem cell-associated heterogeneity in Glioblastoma results from intrinsic tumor plasticity shaped by the microenvironment. Nat Commun. 2019;10:1787.
43. Zhou N, Yuan X, Du Q, Zhang Z, Shi X, Bao J, et al. FerrDb V2: update of the manually curated database of ferroptosis regulators and ferroptosis-disease associations. Nucleic Acids Res. 2022;51:D571–82.
44. Jahani-Asl A, Yin H, Soleimani VD, Haque T, Luchman HA, Chang NC, et al. Control of glioblastoma tumorigenesis by feed-forward cytokine signaling. Nat Neurosci. 2016;19:798–806.
45. Dong M, Wang B, Wei J, de Fonseca AHO, Perry CJ, Frey A, et al. Causal identification of single-cell experimental perturbation effects with CINEMA-OT. Nat Methods. 2023;20:1769–79.
46. Simonds EF, Lu ED, Badillo O, Karimi S, Liu EV, Tamaki W, et al. Deep immune profiling reveals targetable mechanisms of immune evasion in immune checkpoint inhibitor-refractory glioblastoma. J Immunother Cancer. 2021;9:e002181.
47. Kosaka A, Ohkuri T, Okada H. Combination of an agonistic anti-CD40 monoclonal antibody and the COX-2 inhibitor celecoxib induces anti-glioma effects by promotion of type-1 immunity in myeloid cells and T-cells. Cancer Immunol Immunother. 2014;63:847–57.
48. Genoud V, Marinari E, Nikolaev SI, Castle JC, Bukur V, Dietrich P-Y, et al. Responsiveness to anti-PD-1 and anti-CTLA-4 immune checkpoint blockade in SB28 and GL261 mouse glioma models. Oncoimmunology. 2018;7:e1501137.
49. Lindtner S, Catta-Preta R, Tian H, Su-Feher L, Price JD, Dickel DE, et al. Genomic resolution of DLX-orchestrated transcriptional circuits driving development of forebrain GABAergic neurons. Cell Rep. 2019;28:2048-2063.e8.
50. Sun R, Han R, McCornack C, Khan S, Tabor GT, Chen Y, et al. TREM2 inhibition triggers antitumor cell activity of myeloid cells in glioblastoma. Sci Adv. 2023;9:eade3559.
51. Zhang P, Miska J, Lee-Chang C, Rashidi A, Panek WK, An S, et al. Therapeutic targeting of tumor-associated myeloid cells synergizes with radiation therapy for glioblastoma. Proc Natl Acad Sci. 2019;116:23714–23.

52. Barashdi MAA, Ali A, McMullin MF, Mills K. Protein tyrosine phosphatase receptor type C (PTPRC or CD45). J Clin Pathol. 2021;74:548–52.
53. Saunders AE, Johnson P. Modulation of immune cell signalling by the leukocyte common tyrosine phosphatase, CD45. Cell Signal. 2010;22:339–48.
54. Jin S, Guerrero-Juarez CF, Zhang L, Chang I, Ramos R, Kuan C-H, et al. Inference and analysis of cell-cell communication using cell chat. Nat Commun. 2021;12:1088.
55. Kamber RA, Nishiga Y, Morton B, Banuelos AM, Barkal AA, Vences-Catalán F, et al. Inter-cellular CRISPR screens reveal regulators of cancer cell phagocytosis. Nature. 2021;597:549–54.
56. Liu B, Jing Z, Zhang X, Chen Y, Mao S, Kaundal R, et al. Large-scale multiplexed mosaic CRISPR perturbation in the whole organism. Cell. 2022;185:3008-3024.e16.
57. Keys HR, Knouse KA. Genome-scale CRISPR screening in a single mouse liver. Cell Genom. 2022;2:100217.
58. Yang D, Jones MG, Naranjo S, Rideout WM, Min KHJ, Ho R, et al. Lineage tracing reveals the phylodynamics, plasticity, and paths of tumor evolution. Cell. 2022;185:1905-1923.e25.
59. Katti A, Vega-Pérez A, Foronda M, Zimmerman J, Zafra MP, Granowsky E, et al. Generation of precision preclinical cancer models using regulated in vivo base editing. Nat Biotechnol. 2024;42:437–47.
60. Sun N, Petiwala S, Wang R, Lu C, Hu M, Ghosh S, et al. Development of drug-inducible CRISPR-Cas9 systems for large-scale functional screening. BMC Genom. 2019;20:225.
61. Loew R, Heinz N, Hampf M, Bujard H, Gossen M. Improved Tet-responsive promoters with minimized background expression. BMC Biotechnol. 2010;10:81–81.
62. Mueller S, Kline C, Stoller S, Lundy S, Christopher L, Reddy AT, et al. PNOC015: repeated convection-enhanced delivery of MTX110 (aqueous panobinostat) in children with newly diagnosed diffuse intrinsic pontine glioma. Neuro-Oncol. 2023;25:2074–86.
63. Liu H, Gonzalez DD, Viswanath DI, Pol RSV, Saunders SZ, Trani ND, et al. Sustained intratumoral administration of agonist CD40 antibody overcomes immunosuppressive tumor microenvironment in pancreatic cancer. Adv Sci. 2023;10:2206873.
64. Cai H, Zhang B, Ahrenfeldt J, Joseph JV, Riedel M, Gao Z, et al. CRISPR/Cas9 model of prostate cancer identifies Kmt2c deficiency as a metastatic driver by Odam/Cabs1 gene cluster expression. Nat Commun. 2024;15:2088.
65. Martinez S, Wu S, Geuenich M, Malik A, Weber R, Woo T, et al. In vivo CRISPR screens reveal SCAF1 and USP15 as drivers of pancreatic cancer. Nat Commun. 2024;15:5266.
66. McCord M, Bartom E, Burdett K, Baran A, Eckerdt FD, Balyasnikova IV, et al. Modeling therapy-driven evolution of glioblastoma with patient-derived xenografts. Cancers. 2022;14:5494.
67. Ma H, Tu L-C, Naseri A, Huisman M, Zhang S, Grunwald D, et al. CRISPR-Cas9 nuclear dynamics and target recognition in living cells. J Cell Biol. 2016;214:529–37.
68. Banskota S, Raguram A, Suh S, Du SW, Davis JR, Choi EH, et al. Engineered virus-like particles for efficient in vivo delivery of therapeutic proteins. Cell. 2022;185(2):250–265.e16.
69. Gilbert LA, Horlbeck MA, Adamson B, Villalta JE, Chen Y, Whitehead EH, et al. Genome-scale CRISPR-mediated control of gene repression and activation. Cell. 2014;159:647–61.
70. Gilbert LA, Larson MH, Morsut L, Liu Z, Brar GA, Torres SE, et al. CRISPR-mediated modular RNA-guided regulation of transcription in eukaryotes. Cell. 2013;154:442–51.
71. Ozawa T, James CD. Establishing intracranial brain tumor xenografts with subsequent analysis of tumor growth and response to therapy using bioluminescence imaging. J Vis Exp. 2010:(41):1986.
72. Chen P-Y, Ozawa T, Drummond DC, Kalra A, Fitzgerald JB, Kirpotin DB, et al. Comparing routes of delivery for nanoliposomal irinotecan shows superior anti-tumor activity of local administration in treating intracranial glioblastoma xenografts. Neuro-Oncol. 2013;15:189–97.
73. Yin D, Forsayeth J, Bankiewicz KS. Optimized cannula design and placement for convection-enhanced delivery in rat striatum. J Neurosci Methods. 2010;187:46–51.
74. Serwer L, Hashizume R, Ozawa T, James CD. Systemic and local drug delivery for treating diseases of the central nervous system in rodent models. J Vis Exp. 2010:(42):1992.
75. Ozawa T, Faddegon BA, Hu LJ, Bollen AW, Lamborn KR, Deen DF. Response of intracerebral human glioblastoma xenografts to multifraction radiation exposures. Int J Radiat OncolBiolPhys. 2006;66:263–70.
76. Stuart T, Butler A, Hoffman P, Hafemeister C, Papalexi E, Mauck WM III, et al. Comprehensive integration of single-cell data. Cell. 2019;177:1888-1902.e21.
77. Hafemeister C, Satija R. Normalization and variance stabilization of single-cell RNA-seq data using regularized negative binomial regression. Genome Biol. 2019;20:296.
78. Li J, Sheng Q, Shyr Y, Liu Q. scMRMA: single cell multiresolution marker-based annotation. Nucleic Acids Res. 2021;50:gkab931-.
79. Franzén O, Gan LM, Björkegren JLM. PanglaoDB: a web server for exploration of mouse and human single-cell RNA sequencing data. Database. 2019;2019:baz046.
80. Wolock SL, Lopez R, Klein AM. Scrublet: computational identification of cell doublets in single-cell transcriptomic data. Cell Syst. 2019;8:281-291.e9.
81. Blanco-Carmona E. Generating publication ready visualizations for single cell transcriptomics using SCpubr. bioRxiv. 2022;2022.02.28.482303. https://doi.org/10.1101/2022.02.28.482303.
82. Hafemeister C, Halbritter F. Single-cell RNA-seq differential expression tests within a sample should use pseudo-bulk data of pseudo-replicates. bioRxiv. 2023;2023.03.28.534443. https://doi.org/10.1101/2023.03.28.534443.
83. Stuart T, Srivastava A, Madad S, Lareau CA, Satija R. Single-cell chromatin state analysis with Signac. Nat Methods. 2021;18:1333–41.
84. Wolf FA, Angerer P, Theis FJ. SCANPY: large-scale single-cell gene expression data analysis. Genome Biol. 2018;19:15.
85. Kuleshov MV, Jones MR, Rouillard AD, Fernandez NF, Duan Q, Wang Z, et al. Enrichr: a comprehensive gene set enrichment analysis web server 2016 update. Nucleic Acids Res. 2016;44:W90–7.
86. Chen EY, Tan CM, Kou Y, Duan Q, Wang Z, Meirelles GV, et al. Enrichr: interactive and collaborative HTML5 gene list enrichment analysis tool. BMC Bioinformatics. 2013;14:128.

87. Liu SJ. SRA: in vivo perturb-seq dissects oncologic drivers of glioblastoma and its microenvironment. 2023. Available from: Sequence Read Archive PRJNA1005229. https://www.ncbi.nlm.nih.gov/bioproject/?term=(PRJNA1005229).
88. Zou C, Liu SJ. GilbertLabUCSF/gbm_perturb: initial release for publication on genome biology. Zenodo. 2024. https://doi.org/10.5281/zenodo.13638033.

Publisher's Note

Springer Nature remains neutral with regard to jurisdictional claims in published maps and institutional affiliations.